

# TECHNICAL NOTE

D-1168

ACCELERATOR GRID TESTS ON AN ELECTRON-  
BOMBARDMENT ION ROCKET

By William R. Kerslake

Lewis Research Center  
Cleveland, Ohio

NATIONAL AERONAUTICS AND SPACE ADMINISTRATION  
WASHINGTON

February 1962



## NATIONAL AERONAUTICS AND SPACE ADMINISTRATION

TECHNICAL NOTE D-1168

## ACCELERATOR GRID TESTS ON AN ELECTRON-

## BOMBARDMENT ION ROCKET

By William R. Kerslake

## SUMMARY

A systematic investigation of screen-accelerator grids was made with an ion rocket having a 10-centimeter-diameter electron-bombardment ion source. Mercury ion beams of 0.03 to 0.44 ampere were operated at net accelerating voltages of 900 to 6100 volts. A multihole screen-accelerator grid set passed the greatest percent of an ideal plane diode current with a ratio of between-grid spacing to individual hole diameter of approximately 1. Breakdown between the grids occurred at field strengths of 2000 to 3000 volts per millimeter for grid spacings of 1 to 3 millimeters. The accelerator impingement was about 1 percent and caused little erosion of the molybdenum grids, which indicated a grid life of the order of 1000 hours or better. The experimental work was conducted in a bell jar connected to a 5-foot-diameter by 16-foot-long vacuum tank at Lewis Research Center.

## INTRODUCTION

One of the most promising ion rockets to date has been the electron-bombardment source type described in references 1 and 2. These papers present the results of initial testing of this ion rocket, which uses gaseous mercury propellant, a hot filament to emit electrons for ionizing collisions, a magnetic field to increase electron path length, and a grid wire system to accelerate ions. This source can ionize more than 80 percent of the mercury atoms with 500 electron volts per ion in the ion chamber discharge. This value combined with losses due to filament heat, magnetic field coil power input, and grid impingement results in a beam-power to input-power efficiency of about 70 percent at 5000-second impulse. An extension of the initial work including scaling of the engine diameter is discussed in reference 3.

The present report describes the results of an expanded investigation of the accelerator grids used on the second ion rocket engine of reference 2. An initial test using parallel grid plates with matching

holes was found to be more successful than the grid wires previously used. A detailed program was outlined to study various grid plate spacings, hole sizes, and plate thicknesses. A minimum grid spacing of about 2 millimeters was selected from consideration of electrical breakdown, fabrication, and warping problems. A maximum spacing of about 10 millimeters was selected from considerations of space-charge-limited flow in the beam. Most of the investigation was conducted at ion beam currents of 0.125 and 0.25 ampere, although some data were obtained with currents as low as 0.034 ampere and as high as 0.44 ampere. The range of specific impulse investigated was from 3000 to 7800 seconds, while the corresponding net acceleration potential differences were 900 to 6100 volts for singly ionized mercury atoms.

The size of grid holes was designed to be of the order of the grid spacings. Grid holes too large could cause electrical field distortion with attendant reduction of current capacity, while holes too small could also limit current because of cross-sectional blockage. Also, grid impingement due to random motion of the ions would increase as hole size is reduced. The plate thicknesses were chosen thick enough to resist heat warpage and sputtering damage, and yet thin enough to reduce weight and ion impingement.

Data were retaken with the parallel wire grids of reference 2 and are included for comparison. No attempt was made to change the ion source operation; in fact, care was taken to run the ion source at nearly constant conditions for all accelerator data. Future studies of the ion source may improve accelerator performance by supplying to the accelerators a more uniform plasma profile with less neutrals.

## APPARATUS

The ion engine used in these experiments was mounted in a 20-inch-diameter bell jar and fired its beam through a 12-inch valve into a vacuum tank 16 feet long and 5 feet in diameter. Figure 1 shows a cross-sectional view of the vacuum tank, ion engine, cold baffles, ion gage location, neutralizer wire, and button probe. The tank was evacuated by three 32-inch-diameter oil diffusion pumps with liquid-nitrogen cold traps. A more complete description of this tank is found in reference 4 or 5. The neutralizer consisted of a heated tantalum wire strung across the beam about 25 centimeters from the engine.

The movable button probe consisted of an insulated tip of molybdenum 0.4 centimeter in diameter supported by an axial rod extending 45 centimeters from a pivot point. The tip of the probe could be biased from 0 to -200 volts to repel any stray electrons in the tank; a negative bias of about 5 volts was usually enough to obtain a constant current reading when the tip was in the beam. The rod or shaft of the

probe was grounded. Thus the current from the tip should indicate the number of ions striking the tip face, assuming singly charged ions and neglecting secondary electron emission. The maximum error due to secondary electrons was probably less than 10 percent for 4000-electron-volt heavy ions on a molybdenum surface (ref. 6).

The liquid-nitrogen-cooled surfaces contained an area of approximately 33 square meters, which together with the diffusion pumps enabled the tank to be evacuated to  $5 \times 10^{-7}$  to  $9 \times 10^{-7}$  millimeter mercury and the bell jar to  $5 \times 10^{-6}$  to  $9 \times 10^{-6}$ . With the ion engine in operation, the tank pressure was  $2 \times 10^{-5}$  to  $6 \times 10^{-6}$  while the bell jar pressure was  $1 \times 10^{-5}$  to  $3 \times 10^{-5}$  millimeter mercury.

Figure 2 shows a cutaway sketch of the electron-bombardment ion source used throughout the entire program. This source is similar to the second ion rocket engine of reference 2. Gaseous mercury propellant was supplied by a steam-heated boiler and was controlled by one of several calibrated orifices. The surface of the liquid mercury pool was over 200 times the orifice area, so vapor equilibrium should have existed throughout the steam-jacketed boiler. A series of 24 orifice calibrations in which the mercury was weighed before and after a steady flow period gave experimental values within  $\pm 5$  percent of the average. The average flow value was 11 percent higher than a calculated value for free molecular flow through a sharp-edged orifice.

The mercury vapor jet from the orifice impinged on the distributor, which served to provide a relatively uniform influx of vapor to the ion chamber. The ion chamber, about 10 centimeters long, was bounded by a cylindrical anode 10 centimeters in diameter. The emitter, a hairpin-shaped filament of 0.08-centimeter-diameter tungsten, was positioned along the centerline of the ion chamber. Emitted electrons were prevented from reaching the anode directly by the axial magnetic field, which extended their paths to increase the probability of ionizing collisions. The magnetic field coil was so arranged that a divergent field was produced, with a strength of about 22 to 27 gauss at the downstream end (screen) of the ion chamber and 34 to 41 gauss at the upstream end (distributor).

In operation, the energetic electrons from the emitter produced ions by collision, and the chamber became filled with a plasma. The accelerating structure, comprising a screen and an accelerator grid at the downstream end of the chamber, extracted ions from the plasma and accelerated them as a beam. Aluminum oxide balls supporting and insulating the screen and accelerator grids were varied in size (0.475, 0.555, 0.635, and 0.950 cm diam.) to change the spacing between the grids.

Figure 3 and table I present details of 15 screen-accelerator combinations that were tested. Holes in the grids were match-drilled to insure good alignment. Although the grids were fabricated from initially flat plates, some warping occurred during manufacturing, assembly, and engine operation. The parallel grid wire set of configuration 12 or 13 was the same set as that used in reference 2 and had fastenings that permitted axial expansion of the wires to alleviate wire warpage from heat expansion. Configurations 14 and 15 had a chamfer angle cut into the back or downstream side of each hole of the screen to improve the ion optics. The  $33^\circ$  chamfer (configuration 15) was the smallest angle that could be machined and still maintain screen strength using 0.476-centimeter-diameter holes on 0.635-centimeter centers. The  $45^\circ$  chamfer represented a mechanically stronger screen and offered another feasible angle to test.

#### PROCEDURE

Prior to each test, the screen and accelerator grids were weighed, the ion engine was assembled, and the grid spacing was measured at five random locations. The engine was then mounted in the bell jar, which was roughed down, opened to the tank, and permitted to pump down for approximately 1 hour to obtain a  $5 \times 10^{-7}$  to  $9 \times 10^{-7}$  millimeter mercury tank pressure and a  $5 \times 10^{-6}$  to  $9 \times 10^{-6}$  millimeter mercury bell jar pressure. To start the ion engine, mercury propellant flow was turned on by steam-heating the boiler. As the boiler reached temperature (3 to 5 min), the magnetic field, filament current, and anode voltage were turned on. When sufficient density of mercury vapor built up in the ion chamber, the ion chamber discharge started. Ion acceleration was accomplished by raising the positive voltage level of the entire engine except for the accelerator grid, which was lowered. The anode had the highest positive voltage with the screen, distributor, and engine shell electrically tied together 50 volts lower. Figure 4 gives a schematic drawing of the electrical system.

Various combinations of accel-decel voltages were tested with sufficient decel voltage to stop backstreaming electrons. To test for sufficient decel voltage, the accelerator grid voltage was slowly increased (towards ground potential) until the ground return current started to increase, which indicated the start of electron backstreaming. As the ground return meter was the basic measure of beam current, it was important that no electrons be permitted to backstream, since high erroneous values of beam current would be indicated. The filament emission was adjusted slightly to maintain a constant beam current as accel-decel voltages were changed. In addition, the engine was always (excluding run 8) operated at a constant propellant utilization of 0.8 (ion beam out divided by neutral mercury flow in). For configuration 8 the propellant utilization was 0.22.

The ion engine was operated at beam currents from 0.034 to 0.436 ampere with the bulk of the data taken at 1/8- and 1/4-ampere beams. The maximum beam current of 0.436 ampere was used to obtain 0.010-pound thrust at 5000-second specific impulse. Ion chamber performance was held approximately constant with 50 volts difference between the filament and the ion chamber (cathode to anode) and 22- to 27-gauss magnetic field strength at the screen. The filament emission was varied to obtain the required propellant utilization. Emission currents of 1 to 2 amperes were typical for the 1/8-ampere beam; and 3 to 4 amperes for the 1/4-ampere beam. At the end of a run (average length about 2 hr) the screen and accelerator grids were measured for spacing and weight changes.

## RESULTS AND DISCUSSION

While the ion chamber performance was held nearly constant, as described in PROCEDURE, 15 different sets of screen-accelerator grids were tested over the ranges of accel-decel voltages while the impingement current was noted on the second or accelerator grid. Summarized data are given in table II, and table III presents individual data points. Data are plotted in figure 5 for one typical screen-accelerator set and for two different levels of ion beam current. Accelerator impingement current is plotted as a function of  $V_I$ , total voltage on the anode; this is also the net voltage through which the ion is finally accelerated. Curves are shown for constant  $R$  values, where  $R$  is defined as  $V_I/(V_I + |V_A|)$ , the ratio of net-to-total acceleration voltage. (All symbols are defined in appendix A.) Since the accelerator voltage is negative, the absolute value of  $V_A$  must be added to  $V_I$  to obtain the total acceleration potential difference. Impingement curves for the other grid configurations were similar to figure 5 and are not plotted, although the results are included in tables II and III.

### Child's Law Current

For every screen-accelerator grid set tested, there was a region of operation at fairly constant low impingement current for high values of  $V_I$ . As the values of  $V_I$  and  $|V_A|$  were lowered, keeping  $R$  constant, there was a sudden and steep rise in the accelerator impingement current. This sudden rise indicated that the accelerator was becoming space-charge-limited. As the plasma source was held constant, a constant number of ions probably diffused into the accelerator system. When the acceleration voltage was slowly lowered, a point could be reached when the ions were no longer accelerated through the grids as fast as they were received. These accumulated ions might then randomly be repelled by space charge effects and rapidly increase the impingement

on the accelerator grid. Table II lists screen-accelerator grid spacings, the knee (point of rapid increase) of each impingement curve, the breakdown voltage, and the percent of beam impingement at the minimum part of the curve.

The total acceleration voltage at which the accelerators became space-charge-limited was obtained by taking the value of  $V_I$  at the knee of each curve and dividing it by  $R$ . This voltage was used in the Child's law equation to calculate a beam current based on the screen grid open area and distance between the grids. The following form of Child's law was used to calculate saturation beam current between two parallel plates:

$$J_B = \frac{8}{9} \epsilon_0 \sqrt{\frac{q}{2m}} \frac{A_0 (\Delta V)^{3/2}}{l^2} = 0.386 \times 10^{-8} \frac{A_0 (\Delta V)^{3/2}}{l^2}$$

where

$J_B$  saturation beam current, amp

$\Delta V$  total acceleration voltage,  $V_I + |V_A|$ , volts

$l$  acceleration distance between grids, cm

$A_0$  screen grid open area,  $\text{cm}^2$

$\epsilon_0$  permittivity of free space,  $8.85 \times 10^{-12} \frac{\text{coulomb}^2}{\text{newton-meter}}$

$\frac{q}{m}$  charge-to-mass ratio,  $0.4811 \times 10^6 \frac{\text{coulomb}}{\text{kilogram}}$  for  $\text{Hg}^{+1}$  ions

The experimental beam current, expressed as a percent of the calculated ideal Child's law current, is plotted in figure 6 against the ratio of grid spacing to screen hole diameter. The proper grid spacing  $l$  to use was questionable because the thickness of the grids was large compared with the gap between them. Figure 6(a) has been plotted with a grid spacing  $l$  from the middle or centerline of the screen thickness to the middle of the accelerator thickness. Figure 6(b) uses a grid spacing  $l$  that is the actual physical gap between the surfaces. For the wire grid configurations, the open space between wires in the transverse direction was used instead of the hole diameter.

The first trend to be noted in figure 6 and in table II is that performance of the wire grids is lower and separated from the bulk of data for multihole plate grids. The second trend is one of a higher percent of Child's law current as the grid-spacing to hole-diameter ratio increases. The third trend to be pointed out is the general



lowering of percent of Child's law current realizable as  $R$ , the net-to-total accelerating voltage, is lowered for a given configuration (constant grid spacing to hole diameter).

There was no straightforward explanation of the first trend except that the wire, being a two-dimensional approximation, may distort the electric field between the grid plates more than the three-dimensional multihole grids. The second and third trends were interpreted in terms of a grid aperture effect. Using equations for a plane triode with parallel grid wires presented in reference 7, the grid aperture effect may be calculated as a function of grid spacing and geometry. Details of the calculation are presented in appendix B. The result of this calculation modified for the geometry of multihole grid plates is plotted in figure 7 in terms of grid spacing and voltage ratios. Calculated values of the percent of ideal Child's law current also increase as the ratio of grid spacing to hole diameter increases. In addition, as  $R$  is decreased, for a constant ratio of grid spacing to hole diameter, the percent of ideal current again falls as in the experimental values of figure 6.

Comparison of figures 6 and 7 shows the theoretical curves to fall between the experimental sets of data based on two different acceleration distances  $l$ . This alignment should not be taken to mean that the correct acceleration distance is somewhere between the two values of  $l$  chosen, as the calculated values in figure 7 could shift according to assumptions made in converting the plane triode equations to the multihole grid case.

In addition, the calculations are based on the assumption that the ions originate with zero velocity from some equipotential surface (screen grid); this is probably far from the case. The ions passing through the screen grid should possess a substantial velocity (much greater than thermal) and may already be focused by the geometry of the plasma sheath through which they have passed. Unfortunately for analysis, the geometry of the plasma sheath does not constitute an independent variable but will itself undergo modifications as  $V_I$  and  $R$  are changed. Also, there is a possibility that all the configurations have too low experimental values of the percent of Child's law current because the entire grid area was not used effectively. The overall plasma sheath profile might have furnished more ions to the center of the grid than to the outer edges for acceleration.

The scatter in the experimental data of figure 6 is to be expected when considering (1) the many different screen-accelerator configurations included, (2) the tolerances in holding the grids parallel in any one configuration, and (3) the possible errors in picking a "knee value" for the saturation voltage from curves such as those of figure 5. If one configuration is considered at a time and only the screen-accelerator spacing is changed, the change in the percent of Child's law current

does seem to follow the grid aperture effect more closely. Figure 8 shows just two configurations with the calculated grid aperture effect curves. The data for configuration 1 fall almost on the calculated values, while the data for configuration 7 lie parallel to and uniformly above the calculated curves.

### Breakdown Voltages

Before each run and with no propellant flow, the total breakdown voltages of the screen-accelerator grid configurations were measured and found to vary between 6000 and 13,000 volts. The breakdown voltage while the ion engine was operating was generally about two-thirds the no-flow breakdown value but was not always at a definite point. Sometimes the engine would operate for a minute or two, long enough to record a data point, and then voltage breakdown would occur. Attempts to immediately restart the beam at the same voltages were usually unsuccessful, and only a lower voltage point would be stable. The lower breakdown voltage was thought to arise from the increased bell jar pressure caused by the first breakdown. In general, the ion engine would arc at even modest voltages, 2000 to 3000 total volts, when the bell jar pressure rose much above  $4 \times 10^{-5}$  millimeter mercury. The bell jar pressure would rise as the ion engine became hot ( $250^{\circ}\text{C}$ ) during the course of operations. The beam of the ion rocket apparently had a pumping effect on the bell jar, as the ion gage reading would lower by  $1 \times 10^{-5}$  to  $2 \times 10^{-5}$  millimeter mercury when the accelerating voltage was turned on.

Values of breakdown voltages while operating are plotted in figure 9 as a function of the surface-to-surface grid spacing. Not all runs were tested up to breakdown. These runs are listed in table II as having breakdown voltages greater than the maximum voltage tested. The breakdown voltage was higher for higher grid spacings, as expected, and values of field strength at breakdown were typically 2000 to 3000 volts per millimeter for grid spacings of 1 to 3 millimeters. Grid spacings of less than 1 millimeter were not investigated because of the difficulties of fabricating and maintaining such small spacings over a 10-centimeter diameter. Also, these small spacings would probably cause breakdown at voltages too low for the desired operating range of specific impulses.

The scatter of data in figure 9 was probably due to (1) some breakdowns occurring across the insulator balls (rather than the grids) when ball surfaces were partly coated with sputtered metal, (2) breakdown occurring at lower voltages because the grids occasionally were running hot (up to  $1000^{\circ}\text{C}$ ) from high impingement, and (3) thermal distortion altering the grid spacing.

### Impingement and Charge Exchange

In the constant part of the accelerator impingement curve (typical curves shown in fig. 5), the impingement current was generally less than 1.0 percent of the total beam current for the 1/8-ampere beams and 0.9 to 1.7 percent for the 1/4-ampere and greater beams. Most of the 1/8-ampere beam data with more than 1.0 percent impingement was obtained at bell jar pressures greater than  $2 \times 10^{-5}$  millimeter mercury. The minimum beam impingement for all runs, presented in table II and plotted in figure 10, occurred near the knee of the curve and was followed by either a gentle rise or no rise at all in the impingement as  $V_I$  was increased. The impingement data for the non-space-charge-limited case (level portion) were thought to be partly a function of charge exchange between the ion beam and neutral molecules, and a discussion of this interaction follows.

Two sources of neutrals were considered: (1) the 20-percent non-ionized propellant from the ion chamber, and (2) diffusion of molecules from the bell jar or vacuum tank. Ions that lose their charge to neutrals either between the screen and accelerator grids (zone 1 in fig. 4) or in the downstream deceleration region (zone 2 in fig. 4) would contribute to the metered impingement current, as these low-velocity charge-exchanged ions could not escape the negative field of the accelerator. The following equation was used to calculate the percent of the beam undergoing charge exchange:

$$\frac{N}{N_0} = e^{-\sigma n_0 x}$$

where

$N_0$  total number of ions in beam

$N$  number of ions passing through without undergoing charge exchange

$\sigma$  charge-exchange cross section,  $1.2 \times 10^{-14}$  cm<sup>2</sup> (ref. 8)

$n_0$  neutral density, molecules/cm<sup>3</sup>

$x$  distance that ion travels through neutrals, cm

The percent of ions losing their charge would be:

$$\frac{N_0 - N}{N_0} = (1 - e^{-\sigma n_0 x}) 100, \%$$

and, for small values of  $\sigma n_0 x$ ,

$$\frac{N_0 - N}{N_0} \approx (\sigma n_0 x) 100, \%$$

The following table summarizes the calculated percent of beam charge exchanged for run 6 at 0.125-ampere beam current.

Zone	$n_0$ , mol/cm <sup>3</sup>		x, cm	$V_I$ , volts	R	Percent of beam undergoing charge exchange		Impingement current, % of measured beam current
	Engine neutrals	Bell jar neutrals				Engine neutrals	Bell jar neutrals	
1	$3 \times 10^{11}$	$2 \times 10^{11}$	0.403	----	---	0.15	0.10	----
2	$3 \times 10^{11}$	$2 \times 10^{11}$	0	3000	1.0	0	0	0.44
			.656	↓	.8	.24	.16	.56
			1.118	↓	.6	.41	.27	.78
			0	3500	1.0	0	0	.44
			.744	↓	.8	.27	.18	.66
			1.257	↓	.6	.46	.31	.84

It was assumed that  $\sigma$  equals  $1.2 \times 10^{-14}$  square centimeter for all mercury ion velocities from 2000 to 8000 volts. The two values of  $n_0$  were based either on (1) the 20-percent nonionized mercury propellant flowing from the ion chamber at 250° C or on (2) the bell jar ion gage reading of  $1.8 \times 10^{-5}$  millimeter mercury at 25° C. As mercury was assumed to be the major gas constituent, an ion gage correction of one-third (ref. 9) the number of molecules per unit volume was used to calculate  $n_0$  for the bell jar. If the nonionized mercury flowing from the ion chamber were heated by ion chamber collisions to 5 electron volts (58,000° K), the calculated value of  $n_0$  would be lower by a factor of 10 at this higher temperature. The value of  $x$  was the screen-accelerator spacing for zone 1 (fig. 4). The value of  $x$  for zone 2 was calculated by equation (45) of reference 10 using  $V_I$ ,  $R$ , and  $J_B$  and solving for  $x$ , the deceleration distance for space-charge-limited flow between the accelerator and a virtual downstream ground electrode. Equation (45) of reference 10 gives a calculated  $x$  value of 0 for  $R = 1.0$ ; but, in operating the ion rocket in a vacuum tank, a small deceleration distance probably exists between the accelerator at ground potential and a positive space charge of about +30 volts in the plasma of the tank.

The measured accelerator impingement values were a combination of the direct ion impingement plus charge-exchange ions. Because the calculation method was very approximate, it should not be used to deduce the amount of direct impingement but rather to compare trends in the impingement curves as the acceleration and deceleration voltages were varied. It does, however, indicate that up to one-half the total impingement current could be due to charge exchange.

The higher impingement with lower  $R$ , noted in figure 5(a), can be explained by the charge-exchange current increasing as more deceleration voltage was used. A slight increase of impingement with  $V_I$  for each  $R$  curve was a result of a large total-acceleration voltage causing a longer  $x$  for zone 2 and an increase in the percent of charge exchange as noted in the preceding table.

When screen-accelerator grids were run with larger holes in the accelerator, it was expected that impingement might be less because the larger downstream holes would require more random motion of the ions for the same amount of direct impingement. Runs 7 and 11, with larger accelerator holes, showed no noticeable change in impingement current. These runs seem to support the charge-exchange theory as accounting for much of the impingement current, but there is also the possibility that the increased divergence of the electric field spreads the ion flow as the downstream holes are enlarged.

Operation of an ion engine in space could eliminate the contribution of the "bell jar neutrals" to the overall neutral density. Thus, space operation should result in less accelerator impingement current losses and less sputtering damage to the grids.

#### Pierce-Type Grids

In an attempt to improve the ion optics of the multihole grids, each hole in the screen was beveled on the downstream corner to an angle of  $45^\circ$  (configuration 14) and  $33^\circ$  (configuration 15), as shown in figure 3(d). The object of the screen angle was to focus the beam into the accelerator hole and thereby reduce ion impingement on the accelerator. The design followed the general principles derived by Pierce in reference 11, but the actual angles were chosen for mechanical requirements as mentioned in the procedure. Data for these configurations are included in table II, but were not plotted in figure 6 because these screens were a unique geometry change from the unbeveled screen of configurations 1 to 11.

For runs 14 and 15 the accelerator impingement values were the lowest of the entire program (0.2 to 0.4 percent), but at the same time the bell jar pressures were low, which indicated that less charge

exchange should occur. It was difficult experimentally to separate impingement current and charge-exchange current. When the ion rocket was running at low impingement, the accelerator grid was cool and produced less neutrals from sputtering, which resulted in less charge-exchange current. When the ion rocket was running at high impingement, however, the heat of the accelerator grid caused more neutrals to be generated, leading to a higher charge-exchange current. The percent of Child's law current achieved was about the same for the  $45^\circ$  angle screen hole as for the normally drilled screen hole configurations but was about 10 to 15 percent less for the  $33^\circ$  angle screen hole.

### Ion Beam Profiles

The molybdenum-tipped probe described in the section APPARATUS was traversed across the beam, and the resulting current picked up by the tip was plotted on an x-y recorder. The minimum distance of the probe tip from the accelerator grid was 12 centimeters. Beam profiles for various specific impulse or ion voltage levels are shown for configuration 9 in figures 11(a), (b), and (c) and for configuration 14 ( $45^\circ$  angle screen, but also similar for configuration 15,  $33^\circ$  angle screen) in figures 11(d) and (e). The current from the probe tip should indicate the number of ions striking the cross-sectional area of the probe tip. Secondary electrons generated by the ions striking the tip would cause an error in the probe current, but this error was neglected because it would be proportional to the ion current and would not affect the profile. At or above tank (ground) potential the probe current was very sensitive to probe potential, which indicated that electrons were striking the probe. Below -5 volts, where the probe bias was generally held, and to -200 volts, the maximum bias tried, the probe current became insensitive to potential, so that the electron contribution to probe current was probably negligible in this range.

The profiles at low impulse were broad and flat, and at higher impulse they became progressively more peaked at the center. These profiles could be explained by a center-peaked profile exiting from the ion chamber plasma sheath. At high impulse there was enough voltage drop across the grids to accept all the ions at the peak, but at lower impulses the peak was partially cut off because of space charge limitations at the center. To satisfy the operational requirement of constant beam current, the filament emission had to be slightly increased at lower impulses, which increased the plasma concentration arriving at the screen. As the center of the grids was probably already space-charge-limited, only the outer parts could pass more current; and thus the profile was broadened.

### Grid Material and Sputtering

E-1430

Molybdenum appeared to be the best grid material of those tested. The sputtering erosion with tungsten was almost as low as that obtained with molybdenum, but tungsten appeared to have a greater tendency to warp. In view of the fabrication problems, tungsten was considered a poor second choice. The tantalum grids sputtered so excessively that electrical breakdowns were very frequent. Copper grids were tried because of their high thermal conductivity, but the copper accelerator grid when heated by 15-milliampere impingement current became badly warped. Although no data are presented in this report, nonmagnetic stainless-steel grids have been successfully used by a coworker on a similar 10-centimeter-diameter ion engine. As long as the impingement current was kept below about 20 milliamperes, the stainless steel appeared to perform as well as molybdenum. Where large impingement currents and grid heating may occur, however, molybdenum grids should definitely be used.

For a 10-centimeter-diameter ion engine the accelerator grid thickness should be over 0.1-centimeter-thick molybdenum to avoid warping from heat effects and distortion from handling. A grid thickness of 0.13 centimeter in configurations 6 and 7 performed excellently and was not considered excessively heavy. Thinner grids were tested (such as configuration 1), but they warped after running at conditions of moderate impingement. The closest to parallel that a grid set could be assembled, run, and remeasured was  $\pm 0.02$  centimeter, measured at five random locations between the grids. Normally, this deviation might be two to three times higher. As long as the closest points did not arc, there seemed to be no adverse effects due to slightly nonparallel assembly. The grids of configurations 1 and 2 warped enough to touch together under conditions of excessive impingement. As the accelerator grid generally heated and warped more than the screen grid, the screen grid could probably be made of thinner material and still retain its shape.

Sputtering of the screen and accelerator grids was measured by grid weighings before and after a run. Table II presents the accelerator weight loss, the screen weight gain or loss, and the ratio of the actual accelerator weight loss to a calculated weight loss. Calculation of the weight loss involved taking, for each data point, the operating time, the impingement current, and the ion voltage  $V_A + |V_I|$ . Using sputtering rates from references 12 and 13, the calculated loss for each single data point was computed and summed up to obtain the total calculated weight loss of the run.

The sputtering rate for molybdenum is summarized in figure 12 as a function of impact ion energy. The ratio of actual-to-calculated accelerator weight loss varied from 0.9 to 2.9. These data were not taken to

study sputtering but rather as a measure of how long the accelerator grid plate might last. If the grid plates were to wear evenly for a long-duration run, accelerator plate lives of the order of 1000 hours or better were indicated for even the most severely sputtered runs. The length of a single run, up to several hours, was in general not long enough to pinpoint the places of maximum grid wear. A total running time on grid set number 6 of about 20 hours produced more wear or etching at the center, but the actual thickness change measured was less than 0.003 centimeter. Much longer grid lives can be expected when the grids are not operated over a range of high impingement values as was done during this experimental program. Some of the data scatter may be due to the initial vacuum conditioning or sparking period. The weight loss attributed to sparking during the surface cleanup and outgassing was not known but would vary considerably with the handling prior to testing.

The ratio of actual to calculated sputtering rate was generally lower for molybdenum grids than for other materials. Eighty percent of the runs using molybdenum had ratios between 0.9 and 1.45; while copper, tantalum, and tungsten grids averaged 2.0. Tantalum grids caused the most severe breakdowns between the grids of any material tested; these breakdowns were accompanied with a shower of metal sparks from the engine.

The last two runs, 14 and 15, with molybdenum grids had very high sputtering ratios. The actual weight lost was about the same as other runs; but the low bell jar pressure caused less charge-exchange current, and therefore a lower calculated loss resulting in a higher ratio of actual to calculated sputtering.

#### CONCLUDING REMARKS

In an evaluation of accelerator grid structures for a 10-centimeter-diameter electron-bombardment ion engine, the percent of Child's law current passed by the grids increased as the ratio of grid spacing to hole diameter increased. This percentage was generally lowered as  $R$ , the ratio of net-to-total accelerating voltage, was reduced. It was also lower for wire grids than for multihole grids at the same ratio of grid spacing to dimension of opening (hole diameter for plates, and clear space between wires for wire grids). With the accelerator impingement usually less than 1 percent of the total beam current, accelerator grid lives of the order of 1000 hours were indicated if the grid plates were to wear evenly.

The maximum current through a set of grids was obtained by using a minimum spacing between grids and minimum hole size. Even with grids of molybdenum, the best of the materials tested, the surface grid spacing should be no less than 1 millimeter because of fabrication and warpage



problems. At high impulses this distance may have to be increased because of electrical breakdown occurring at 2000 to 3000 volts per millimeter. The ratio of grid spacing to hole diameter should be about 1.5 or less to reduce impingement and greater than 0.6 to avoid electric field distortion. The selection of hole size may also involve the ion chamber, in that smaller holes may be less efficient for ion extraction.

Lewis Research Center

National Aeronautics and Space Administration

Cleveland, Ohio, October 2, 1961

E-1430

## APPENDIX A

## SYMBOLS

$A_0$	screen grid open area, $\text{cm}^2$
$a$	distance between grid wires of a triode, cm
$B$	axial magnet field at screen, gauss
$d$	distance between accel-decel planes, cm
$J$	current, amp
$l$	acceleration distance between grids, cm
$N$	number of ions not charge-exchanged
$N_0$	total number of ions in beam
$n_0$	neutral density per $\text{cm}^3$
$q/m$	charge-to-mass ratio, $0.4811 \times 10^6$ coulomb/kg for $\text{Hg}^{+1}$
$R$	ratio of net-to-total acceleration voltage, $V_I/(V_I +  V_A )$
$S$	screening fraction of a triode
$V$	potential, volts
$\Delta V$	total acceleration voltage, $V_I +  V_A $
$x$	distance that ion travels through neutrals, cm
$\epsilon_0$	permittivity of free space, $8.85 \times 10^6 \frac{\text{coulomb}^2}{\text{newton-meter}}$
$\mu$	amplification factor of a triode
$\sigma$	charge-exchange cross section, $\text{cm}^2$

## Subscripts:

A	accelerator
B	beam

F	filament
I	anode
1	plane of screen grid
2	plane of accelerator grid
3	plane of virtual decelerator

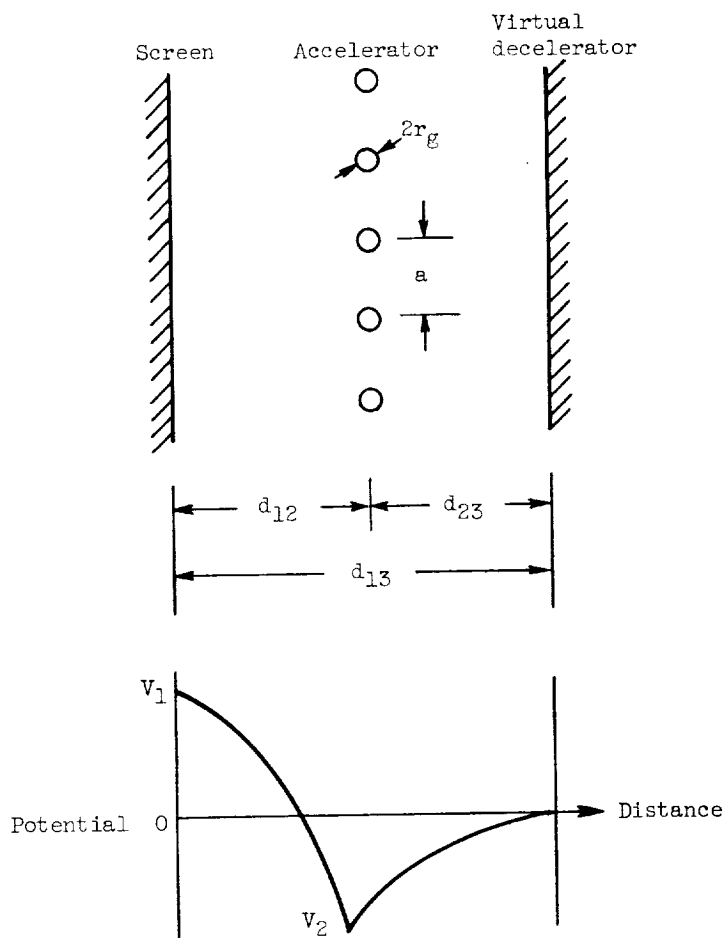
## APPENDIX B

## GRID APERTURE EFFECT

As discussed in reference 7 and given by equation (5) of reference 14, the actual space-charge-limited current  $J_{\text{act}}$  for plane triodes with parallel wire grids is

$$\frac{J_{\text{act}}}{J_{\text{ideal}}} = \left[ \frac{\mu + \frac{V_1}{V_1 - V_2}}{\mu + \left(\frac{d_{13}}{d_{12}}\right)^{4/3}} \right]^{3/2} \quad (\text{B1})$$

where  $J_{\text{ideal}}$  is the space-charge-limited current for a plane diode with spacing  $d_{12}$ ; and  $V_1$ ,  $V_2$ , and  $d_{13}$  are defined in the following diagram.



The amplification factor  $\mu$  in equation (B1) was calculated from equation (7.69) in reference 7.

$$\mu = \frac{\ln \cosh \pi S - 2\pi \frac{d_{23}}{a}}{\ln \tanh \pi S - \ln \left[ 1 - \cosh^2 \pi S \exp \left( \frac{-4\pi d_{23}}{a} \right) \right]} \quad (\text{B2})$$

The following assumptions were made to estimate qualitatively  $\mu$  for a multihole grid configuration:

(1)  $d_{12} = d_{23}$ , the acceleration gap between grid plates, equals the downstream deceleration length.

(2)  $a$ , the grid wire spacing, equals the diameter of a hole in the multihole grid plate.

(3)  $S$ , the screening fraction, is the web thickness between grid holes divided by the sum of the hole diameter plus the web thickness. The screening fraction  $S$  was calculated for accelerator grid configuration 6 to be 0.15.

With  $\mu$  estimated for the multihole grids from equation (B2), the percent of ideal Child's law current was calculated from equation (B1) by using:

$V_1 = V_I$ , voltage on anode of ion engine

$V_2 = V_a$ , voltage on accelerator grid

$$R = \frac{V_I}{V_I + |V_a|}$$

$\frac{d_{12}}{a}$  = Ratio of grid spacing to hole diameter

$d_{13} = 2d_{12}$ , because  $d_{12} = d_{23}$  was assumed

These calculations are plotted in figure 7 for a range of  $\mu$  and  $R$  values. For easier comparison with experimental data,  $d_{12}/a$  is plotted as the abscissa instead of  $\mu$ .

## REFERENCES

1. Kaufman, Harold R.: An Ion Rocket with an Electron-Bombardment Ion Source. NASA TN D-585, 1961.
2. Kaufman, H. R., and Reader, P. D.: Experimental Performance of an Ion Rocket Employing an Electron-Bombardment Ion Source. Paper 1374-60, Am. Rocket Soc., Inc., 1960.
3. Reader, Paul D.: Experimental Effects of Scaling on the Performance of Ion Rockets Employing Electron-Bombardment Ion Sources. Paper presented at Nat. IAS-ARS Joint meeting, Los Angeles (Calif.), June 1961.
4. Childs, J. H.: Design of Ion Rockets and Test Facilities. Paper 59-103, Inst. Aero. Sci., 1959.
5. Keller, Thomas A.: NASA Electric Rocket Test Facilities. Paper R-25, Nat. Vacuum Symposium, 1960.
6. Brunèè, Curt: Über die Ionenreflexion und Sekundärelektronenemission beim Auftreffen von Alkaliionen auf reine Molybdän-Oberflächen. Zs. Phys., bd. 147, no. 5, 1957, pp. 161-183.
7. Spanenberg, Karl Ralph: Vacuum Tubes. McGraw-Hill Book Co., Inc., 1948.
8. Iovitsu, Popescu, and Ionescu-Pallas, N.: Resonant Charge-Exchange and the Kinetics of Ions. Soviet Phys.-Tech. Phys., vol. 4, no. 7, 1960, 781-791.
9. Dushman, S.: Scientific Foundations of Vacuum Techniques. John Wiley & Sons, Inc., 1949.
10. Kaufman, Harold R.: One-Dimensional Analysis of Ion Rockets. NASA TN D-261, 1960.
11. Pierce, J. R.: Rectilinear Electron Flow in Beams. Jour. Appl. Phys., vol. 11, no. 8, Aug. 1940, pp. 548-554.
12. Wehner, G. K., and Rosenberg, D.: Mercury Ion Beam Sputtering of Metals at Energies of 4 to 15 kev. Jour. Appl. Phys., vol. 32, no. 5, May 1961, pp. 887-890.
13. Massey, H. S. W., and Burhop, E. H. S.: Electronic and Ionic Impact Phenomena. Clarendon Press (Oxford), 1956, p. 584.
14. Mickelsen, William R.: Electric Propulsion for Space Flight. Aerospace Eng., vol. 19, no. 11, Nov. 1960, pp. 6-11; 36.

TABLE I. - DIMENSION DETAILS OF SCREEN-ACCELERATOR GRIDS USED ON 10-CENTIMETER-DIAMETER ELECTRON-BOMBARDMENT ION SOURCE

Grid set	Hole diameter, cm		Equilateral triangular hole spacing, cm	Grid thickness, cm	Material	Screen open area, cm <sup>2</sup>	Reference figure
	Screen	Accelerator					
1	0.476	0.476	0.635	0.051	Molybdenum	40.0	3(a)
2				.076			
3				.102	Tungsten		
4				.086	Tantalum		
5				.081	Copper		
6			.559	.130	Molybdenum	52.0	3(b)
7			.635	.130		40.0	3(a)
8		.515	1.270	.051			
9	.952	.952	.423	.127			
10	.315	.315	.315	.076			
11	.238	.238	.635	.051		17.8	3(b)
12	.315	.315					
13	.159 wire	.159 wire	On 0.508 spacing		Tungsten	54.0	3(d)
14	.159 wire	.102 wire					
15	.476	.476	.635	.127 .112 (S) .130 (A)	Molybdenum	40.0	3(c) (45°) 3(c) (33°)





[ $\Delta V_T = -50$  volts for all runs.]

Run	V <sub>I</sub> , volts	V <sub>A</sub> , volts	J <sub>B</sub> , amp	J <sub>A</sub> , amp x10 <sup>3</sup>	J <sub>I</sub> , amp	J <sub>F</sub> , amp	B at screen, gauss	Bell jar pressure, mm Hg x10 <sup>5</sup>	R
1(a)	3500 3000 2750	0 ↓	0.245	5.0 4.6 7.4	3.4 2.8 2.6	2.6 2.8 2.6	22	3.5 3.0 3.5	1.0 ↓
	2500 2200 2100	-1000 -900 -840		3.8 5.4 7.6	↓ 3.6 3.8	2.5 2.9 2.8		2.6 2.8 2.8	.72 ↓
	3000 2500 2000 1800 1 00	-2000 -1700 -1330 -1285 -1200		2.7 2.6 4.6 5.5 7.8	3.1 3.2 3.8 ↓ ↓	2.4 2.4 3.0 ↓ ↓		2.5 2.5 2.6 ↓	.6 ↓
1(b)	5000 5000 4000 3750 3500	-2400 -2000 -1800 -1500 -1400	0.245	3.0 2.9 6.1 8.3 13.0	3.1 3.5 3.7 3.8 4.2	2.0 2.6 2.8 2.9 3.2	22	2.4 2.4 2.3 2.3 2.2	0.72
2	3500 3000 2500 2500 2400 2250 2000	-1400 -1200 -1000 -1000 -900 -900 -800	0.125	1.6 1.5 1.9 2.0 3.8 10.0 18.0	1.8 ↓ ↓ ↓ ↓ ↓ ↓	1.1 1.2 1.6 1.2 1.6 ↓ ↓	23	2.0 1.8 1.7 2.1 2.0 ↓ ↓	0.72 ↓
	3500 3000 2500 2100 2000 1800	-2320 -2000 -1660 -1400 -1330 -1200		2.3 2.3 2.1 2.4 4.2 6.5	↓ 1.1 ↓ ↓ ↓ ↓	↓ ↓ ↓ ↓ ↓ ↓		2.1 2.1 2.2 ↓ ↓ ↓	.6 ↓
	2000 1600 1500 1400 1300 1200 1000	-3000 -2400 -2250 -2100 -1950 -1800 -1500		2.6 2.6 2.6 4.7 6.3 13 40	1.4 ↓ 1.1 1.3 1.3 1.4 1.4	1.0 1.3 ↓ 22 ↓ ↓ ↓		↓ ↓ ↓ ↓ ↓ ↓ ↓	.4 ↓
3(a)	3500 3000 2500 2000 1900 1700 1600 1500	-1400 -1200 -1000 -900 -720 -680 -640 -600	0.125	2.0 2.0 1.6 2.2 2.3 3.7 5.3 11.0	1.5 ↓ ↓ ↓ ↓ ↓ ↓ ↓	1.0 1.1 1.1 1.2 ↓ ↓ ↓ ↓	22	2.7 ↓ ↓ ↓ ↓ ↓ ↓ ↓	0.72 ↓
	3000 2400 1900 1800 1500 1400 1300	-2000 -1800 -1200 -1070 -1000 -930 -870		2.8 2.8 2.5 2.4 3.8 5.0 7.5	↓ 1.2 ↓ ↓ ↓ ↓ ↓	↓ ↓ ↓ ↓ ↓ ↓ ↓		↓ ↓ ↓ ↓ ↓ ↓ ↓	↓
	1400 1200 1100 1000 900	-2100 -1800 -1650 -1500 -1350		3.0 2.8 2.8 4.3 9.3	↓ ↓ ↓ ↓ ↓	↓ ↓ ↓ ↓ ↓		↓ ↓ ↓ ↓ ↓	↓
	4000 3500 3000 2500	-1800 -1400 -1200 -1000	0.250	2.7 2.7 3.0 8.5	5.0 ↓ ↓ ↓	2.8 2.8 3.5 4.5		2.3 ↓ ↓ ↓	.72 ↓
3(b)	4000 3700 3600 3500 3400 3000	-1600 -1450 -1440 -1400 -1360 -1200	0.250	3.8 4.0 4.2 5.7 7.2 4.0	4.2 ↓ ↓ ↓ ↓ ↓	3.2 ↓ ↓ ↓ ↓ ↓	22	2.5 ↓ ↓ ↓ ↓ ↓	0.72 ↓
	4000 3500 3300 3100 3000 2800	-2870 -2330 -2200 -2070 -2000 -1940		3.3 4.8 4.4 4.6 6.1 8.2	5.0 ↓ ↓ ↓ ↓ ↓	3.0 ↓ ↓ ↓ ↓ ↓		↓ ↓ ↓ ↓ ↓ ↓	↓
4	3000	-1000	0.250	6	4.0	3.2	23	2.7	0.75
5	3500 3000 3000 2500 2500 2500	-2000 -2000 -1500 -2000 -1500 -1000	0.135	1.03 1.05 1.23 1.18 1.20 0.90	1.5 ↓ ↓ ↓ ↓ ↓	1.2 ↓ ↓ ↓ ↓ ↓	25	2.4 2.4 2.6 3.0 ↓	0.75

TABLE III. - Continued. INDIVIDUAL DATA POINTS OF THE PERFORMANCE DATA OF TABLE II

[ $\Delta V_I = -50$  volts for all runs.]

Run	$V_I$ , volts	$V_A$ , volts	$J_B$ , amp	$J_A$ , amp $\times 10^3$	$J_I$ , amp	$J_F$ , amp	B at screen, gauss	Bell jar pres- sure, mm Hg $\times 10^5$	R	Run	$V_I$ , volts	$V_A$ , volts	$J_B$ , amp	$J_A$ , amp $\times 10^3$	$J_I$ , amp	$J_F$ , amp	B at screen, gauss	Bell jar pres- sure, mm Hg $\times 10^5$	R	
C	4000	0	0.125	0.60	1.8	1.6	22	1.7	1.0	6	2500	-2500	0.241	3.7	3.7	3.0	22	2.4	0.5	
	3500			.52	1.8	1.6		1.7			2250	-2250		3.5	3.7	2.9		2.4		
	3000			.55	1.9	1.7		1.9			2000	-2000		3.3	4.0	3.4		2.2		
	2700			.60	1.9	1.7					1830	-1830		4.3	4.3	3.8		2.3		
	2500			1.40	2.1	2.0					1700	-1700		9.1	4.8	3.9		2.4		
	2500			1.8	2.1	1.9		2.0			1600	-1600	20	5.8	5.0			2.3		
	2300			6.3	2.3	2.2		1.8			2000	-3000		4.1	3.6	2.8		2.4	.4	
											1670	-2500		3.7	3.8	3.1		2.5		
	3500	-875		.82	1.6	1.4		1.6	.8		1430	-2150		5.9	4.2	3.5		2.5		
	3000	-750		.70	1.8	1.6		1.8			1400	-2100	10	4.8	3.9		2.6			
	2500	-625		.70	2.0	1.8					1330	-2000	.230	40	5.7	5.0		2.4		
	2200	-550		.91	2.4	2.2														
	2000	-500		2.8	2.4	2.2		1.9			4500	-1125	.308	2.8	5.8	4.6		1.5	.8	
	1800	-475		8.2	2.6	2.6		1.8			4000	-1000		2.8	5.8	4.6				
											3500	-875		2.9	6.0	5.2		1.6		
	3500	-2330		1.05	1.5	1.3		1.4	.6		3200	-800		6.4	6.5	5.3		1.6		
	3000	-2000		.98	1.6	1.4					3000	-750	.300	20	7.0	5.3		1.5		
	2500	-1660		.92	1.7	1.55														
	2000	-1330		.90	2.0	1.85					3300	-2200	.308	3.5	5.2	4.3			.6	
	1800	-1200		.92	2.1	1.9					3000	-2000		3.4	5.7	4.7				
	1650	-1100		.94	2.2	2.2					2400	-1600		8.2	6.6	5.3		1.7		
	1570	-1050		1.42	2.4	2.3					2100	-1400	.280	20	6.6	5.3		1.9		
	1500	-1000		5.5	2.6	2.6														
	1500	-1000		9.6	2.8	2.7					2000	-3000	.308	4.0	5.2	4.1		2.0	.4	
											1670	-2500		6.6	5.8	4.8				
	2000	-3000		.96	1.8	1.35		1.2	.4		1530	-2300		11.0	6.2	5.2				
	1670	-2500		1.00	1.6	1.4					1400	-2100	.260	18	6.4	5.4				
	1330	-2000		.85	1.9	1.8														
	1200	-1800		.91	2.1	2.0					7(a)	4500	0	0.125	0.72	1.4	1.1	22	3.2	1.0
	1100	-1650		1.3	2.2	2.1						3500			.64	1.6	1.3		3.2	
	1000	-1500		7.1	2.5	2.5						2500			.60	2.0	1.7		3.4	
												2200			.57	2.4	2.1		2.5	
	1285	-3000		1.1	1.6	1.4			.3			2100			1.00	2.4	2.1		2.5	
	1070	-2500		1.6	1.8	1.75						2000			6.3	2.8	2.5		2.7	
	940	-2200		1.6		1.7														
	800	-2100		30		1.7						3500	-875		.83	1.7	1.4		2.2	.8
												3000	-750		.83	1.8	1.4		2.3	
	4500	-1125	.241	2.5	3.3	2.5		2.2	.8			2000	-500		.80	2.0	1.8		2.4	
	4000	-1000		3.4	3.4	2.6		3.1				1700	-425		.88	2.3	2.1		2.3	
	3500	-875		2.3	4.1	3.4		2.0				1600	-400		4.1	2.8	2.5		2.2	
	3370	-840		3.8	4.1			2.1				1500	-375		8.4	2.8	2.6			
	3200	-800		6.5	4.2			2.2												
	3000	-750		18.0	4.5	3.9		2.2				3000	-2000		1.0	1.7	1.4			.6
												2000	-1330		.89	2.0	1.8			
	3300	-2200		3.15	3.6	3.0		2.0	.6			1500	-1000		.88	2.4	2.2		2.3	
	3000	-2000		3.2	3.7	3.0		2.0				1300	-870		1.0	2.6	2.4		2.3	
	2500	-1870		3.4	3.9	3.1		2.1				1200	-800		5.0	3.0	2.8		2.4	
	2570	-1710		4.7	4.0	3.2		2.2				2000	-3000		1.1	1.7	1.4		1.9	.4
	2400	-1600		8.4	4.2	3.4		2.3												

TABLE III. - Continued. INDIVIDUAL DATA POINTS OF THE PERFORMANCE DATA OF TABLE II

[ $\Delta V_I = -50$  volts for all runs.]

Run	V <sub>I</sub> , volts	V <sub>A</sub> , volts	J <sub>B</sub> , amp	J <sub>A</sub> , amp x10 <sup>3</sup>	J <sub>I</sub> , amp	J <sub>F</sub> , amp	B at screen, gauss	Bell jar pres- sure, mm Hg x10 <sup>5</sup>	R	Run	V <sub>I</sub> , volts	V <sub>A</sub> , volts	J <sub>B</sub> , amp	J <sub>A</sub> , amp x10 <sup>3</sup>	J <sub>I</sub> , amp	J <sub>F</sub> , amp	B at screen, gauss	Bell jar pres- sure, mm Hg x10 <sup>5</sup>	R
7(a)	1600 1200 1000 900	-2400 -1800 -1500 -1350	0.125 ↓ ↓ ↓	1.0 .93 1.1 5.0	1.8 2.1 2.4 2.8	1.8 1.8 2.1 2.4	22	1.8 1.9 2.0 2.0	0.4 ↓ ↓ ↓	9	1400 1000 900 800 700	-2100 -1500 -1350 -1200 -1050	0.125 ↓ ↓ ↓ ↓	4.3 4.0 3.6 7.1 14.4	---- ---- ---- ---- ----	1.3 2.1 2.5 2.5 2.6	22	3.1 3.0 2.8 2.7 2.6	0.4 ↓ ↓ ↓ ↓
	1200 1100 1000 950 900	-2800 -2570 -2330 -2200 -2100	↓ ↓ ↓ ↓ ↓	.99 1.01 1.8 9.0 3.0	1.9 2.0 2.0 2.7 3.0	1.6 1.7 1.7 2.0 2.3		1.7 1.7 1.8 1.9 1.9	.3 ↓ ↓ ↓ ↓		3500 3000 2500 2300 2200 2100 2000	-875 -750 -625 -575 -550 -525 -500	.250 ↓ ↓ ↓ ↓ ↓ ↓	2.1 2.2 2.3 3.0 4.6 7.4 13	---- ---- ---- ---- ---- ---- ----	5.0 5.3 6.3 5.0 5.0 6.0	3.0 ↓ 5.4 3.1 ↓	.8 ↓ ↓ ↓ ↓ ↓ ↓	
	3800 3000 2700 2600 2500	-900 -750 -675 -650 -625	↓ ↓ ↓ ↓ ↓	.243 3.3 3.0 3.7 5.2 9.4	3.5 4.8 4.9 ↓ ↓ ↓	2.0 2.9 3.5 ↓ ↓ ↓		2.4 2.4 2.5 ↓ ↓ ↓	.8 ↓ ↓ ↓ ↓ ↓		2250 1800 1700 1600 1500	-1500 -1200 -1130 -1070 -1000	↓ ↓ ↓ ↓ ↓	2.5 2.5 2.7 8.4 8.5	---- ---- ---- ---- ----	5.3 6.0 ↓ ↓ ↓	2.1 2.1 2.2 2.1 2.1	.8 ↓ ↓ ↓ ↓	
	3750 3000 2500 2100 2000 1900	-2500 -2000 -1670 -1400 -1330 -1270	↓ ↓ ↓ ↓ ↓ ↓	4.4 3.1 3.0 4.4 7.6 10.0	3.7 3.9 4.2 4.4 4.8 5.0	2.8 3.1 3.4 3.6 3.8 4.0		2.2 2.2 2.3 2.4 2.5 2.6	.6 ↓ ↓ ↓ ↓ ↓		1600 1400 1200 1100 1000	-2400 -2100 -1800 -1650 -1500	↓ ↓ ↓ ↓ ↓	3.7 3.7 3.8 6.0 17.3	---- ---- ---- ---- ----	↓ ↓ ↓ ↓ ↓	2.4 2.4 2.5 ↓ ↓	.4 ↓ ↓ ↓ ↓	
	2000 1800 1550 1500 1400	-3000 -2400 -2310 -2250 -2100	↓ ↓ ↓ ↓ ↓	3.9 4.0 4.1 7.5 34	4.0 4.4 4.5 4.5 5.7	3.2 3.5 3.6 3.6 5		2.4 2.9 2.9 3.1 2.8	.4 ↓ ↓ ↓ ↓		4500 3800 3000 2900 2800 2700 2500	-1150 -950 -750 -725 -700 -675 -625	.436 ↓ ↓ ↓ ↓ ↓ ↓	4.1 4.1 4.5 5.1 8.5 10 18	10.0 10.0 10.0 12.0 11.5 11.5 11.0	8.0 8.0 9.4 10.4 10.0 10.0 10.5	29 29 31 ↓ ↓ ↓ ↓	2.0 2.0 2.7 2.7 2.6 2.7 2.7	.8 ↓ ↓ ↓ ↓ ↓ ↓
8	4500 3500 3500	-1000	0.032 .034 .050	8 16 80	0.4 .8 2.6	0.4 0.6 2.2	22	1.6 1.2 2.2	0.78										
9	3000 2000 1700 1600 1500 1400 1300	-750 -500 -425 -400 -375 -350 -325	0.125 ↓ ↓ ↓ ↓ ↓ ↓	1.1 .86 .92 1.3 2.0 3.0 9.2	--- --- --- --- --- --- ---	2.0 3.4 3.9 4.3 4.4 4.5 4.7	22	1.0 ↓ ↓ ↓ ↓ ↓ ↓	0.8 ↓ ↓ ↓ ↓ ↓ ↓		4000 3000 2500 2500 2250	-1600 -1200 -1000 -1000 -900	↓ ↓ ↓ ↓ ↓	4.0 4.0 5.8 11.0 29	↓ ↓ ↓ ↓ ↓	9 10 9.8 9.5 10	↓ ↓ ↓ ↓ ↓	5.0 3.0 3.0 3.2 3.0	.6 ↓ ↓ ↓ ↓
	2700 1800 1500 1300 1200 1100 1600	-1800 -1200 -1000 -860 -800 -730 -2700	↓ ↓ ↓ ↓ ↓ ↓ ↓	2.2 2.0 2.1 2.3 5.3 10 4.8	--- --- --- --- --- --- ---	2.0 2.1 2.3 2.4 2.5 2.7 1.3		↓ 1.6 ↓ ↓ ↓ ↓ 3.2	.6 ↓ ↓ ↓ ↓ ↓ ↓		2200 2000 1900 1800 1750	0 ↓ ↓ ↓ ↓	0.250 ↓ ↓ ↓ ↓	3.1 3.1 4.9 6.7 8.7	3.4 4.4 ↓ ↓ ↓	2.6 3.4 ↓ ↓ ↓	22	3.4 3.8 ↓ ↓ ↓ ↓ 2.2	1.0 ↓ ↓ ↓ ↓ ↓ ↓
	2000 1600 1500	-500 -400 -375	↓ ↓ ↓	3.6 2.6 4.2	3.6 4.3 4.2	2.8 3.8 3.4		↓ ↓ ↓	.8 ↓ ↓										

TABLE III. - Continued. INDIVIDUAL DATA POINTS OF THE PERFORMANCE DATA OF TABLE II  
 $[\Delta V_I = -50 \text{ volts for all runs.}]$

Run	V <sub>I</sub> , volts	V <sub>A</sub> , volts	J <sub>B</sub> , amp	J <sub>A</sub> , amp ×10 <sup>3</sup>	J <sub>I</sub> , amp	J <sub>F</sub> , amp	B at screen, gauss	Bell jar pres- sure, mm Hg ×10 <sup>5</sup>	R	Run	V <sub>I</sub> , volts	V <sub>A</sub> , volts	J <sub>B</sub> , amp	J <sub>A</sub> , amp ×10 <sup>3</sup>	J <sub>I</sub> , amp	J <sub>F</sub> , amp	B at screen, gauss	Bell jar pres- sure, mm Hg ×10 <sup>5</sup>	R		
10	1400	-350	0.250	9.0	5.0	4.2	22	2.2	0.8	12	1400	-2100	0.125	3.9	1.3	1.2	25	1.1	0.4		
	2250	-1500		4.8	2.8	2.0		3.4	.6		1300	-1950	.125	6.5	1.3	1.2		1.1	.4		
	1500	-1000		3.4	3.7	2.8		2.6			5500	-1375	.250	2.6	2.7	2.2		2.6	.8		
	1350	-900		3.9	3.8	3.0		4.0			5000	-1250		4.2	2.8	2.2		2.6			
	1300	-865		4.4	3.8	3.0					4800	-1200		6.0	2.9	2.3		2.6			
	1200	-800		17	4.0	3.2															
	2000	-2000		3.2	3.0	2.6		2.2	.5		4600	-1150		9.5	2.9	2.3		2.6			
	1500	-1500		3.1	3.2	2.5					4400	-1100		15.0	2.9	2.3		2.8			
	1200	-1200		3.0	3.9	3.2					4000	-1000		31	3.0	2.5		2.7	.6		
	1100	-1100		3.4	3.9	3.2		2.3			4200	-2800		4.6	2.8	2.3		2.5			
	1000	-1000		6.3	4.5	3.8		2.2			3900	-2600		12.5	2.8	2.3		3.4			
											3750	-2500		14.0	2.9	2.3		3.0			
	1400	-2100		3.1	3.0	2.3		2.3	.4		13	6000	0	0.125	0.75	1.0		0.8	22	2.3	1.0
	1000	-1500		4.6	3.8	3.2						5000			.61	1.1		.9			
	900	-1350		5.4	4.1	3.5						4000			.55	1.2		1.0			
	600	-1200		13.7	4.6	3.9						3750			.93	1.4		1.2			
							3600			2.2		1.5	1.3								
							3500			2.6											
							3400			3.2											
							3300			4.8											
							3200			6.4				2.2							
							4400	-1100		.79		1.4	1.2		.8						
							4000	-1000		.72		1.4	1.2								
							3600	-900		.69		1.5	1.3	2.4							
							3200	-800		.88			1.3	2.4							
							3000	-750		1.85			1.4	2.3							
							2900	-725		2.4				2.3							
							2800	-700		3.0				2.4							
							2600	-675		6.6				2.3							
11	2750	-688	0.125	0.8	5.8	4.6	20	2.5	0.8	3900	-2600		1.15	1.4	1.2	23		.6			
										3000	-2000		.91	1.4	1.2						
12	4000	0	0.125	0.6	1.3	1.2	25	1.1	1.0	2400	-1600		1.35	1.6	1.4		2.2				
	3600			1.0						2300	-1530		1.64				2.3				
	3500			1.3						2250	-1500		2.2				2.2				
	3400			2.0						2100	-1400		4.1				2.2				
	3300			3.6						2000	-1330		6.1								
	3200			5.4																	
	3000			9.0																	
	4000	-1000		.84	1.1	1.0			.8	2000	-3000		1.05	1.4	1.2		2.0	.4			
	3000	-750		.90	1.3	1.2				1800	-2700		1.00	1.5	1.3						
	2900	-725		1.50						1700	-2550		1.05	1.6	1.4						
	2800	-700		1.74						1600	-2400		2.05								
	2700	-675		3.6						1500	-2250		3.1								
	2600	-650		3.5						1400	-2100		5.4								
	2500	-625		7.0																	
	4500	-3000		2.1	1.0	.9			.6												
	3900	-2600		1.5	1.0	.9															
	3000	-2000		1.0	1.1	1.0															
	2400	-1600		.81	1.3	1.2															
	2300	-1530		.89	1.3	1.2															
	2200	-1460		1.72	1.4	1.3															
	2100	-1400		3.5																	
	2000	-1330		4.8																	
	2000	-3000		1.10	1.1	1.0			.4												
	1800	-2700		.98	1.2	1.1															
	1600	-2400		1.00	1.3	1.2															
	1500	-2250		1.4	1.3	1.2															

TABLE III. - Concluded. INDIVIDUAL DATA POINTS OF THE

PERFORMANCE DATA OF TABLE II

[ $\Delta V_I = -50$  volts for all runs.]

Run	$V_I$ , volts	$V_A$ , volts	$J_B$ , amp	$J_A$ , amp $\times 10^3$	$J_I$ , amp	$J_F$ , amp	B at screen, gauss	Bell jar pres- sure, mm Hg $\times 10^5$	R
14	4000	-1000	0.125	0.28	1.7	1.4	21	1.9	0.8
	3500	-875		.24	↓	↓	22	1.7	↓
	3000	-750		.23	↓	↓	22	1.6	↓
	2700	-675		.30	↓	↓	↓	1.9	↓
	2600	-650		.37	↓	↓	↓	↓	↓
	2500	-625		.60	↓	↓	↓	↓	↓
	2400	-600		1.62	↓	↓	↓	↓	↓
	2300	-575		2.40	↓	↓	↓	1.6	↓
	2550	-1700		.34	↓	1.6	20	1.4	.6
	2100	-1400		.29	1.8	↓	20	1.4	↓
	2000	-1300		.40	↓	↓	21	1.3	↓
	1900	-1270		.82	↓	↓	↓	1.4	↓
	1800	-1200		2.00	↓	↓	↓	1.4	↓
	1500	-2250		.46	↓	↓	↓	1.3	.4
	1400	-2100		.46	↓	↓	↓	↓	↓
	1300	-1950		.50	↓	↓	↓	↓	↓
	1300	-1950		.45	↓	↓	↓	↓	↓
	1200	-1800		2.28	↓	1.5	↓	↓	↓
15	5000	0	0.125	0.19	1.5	1.2	26	1.1	1.0
	4500	↓		.54	↓	↓	↓	↓	↓
	4400	↓		.75	↓	↓	↓	↓	↓
	4250	↓		1.27	↓	↓	↓	↓	↓
	4000	↓		2.37	↓	↓	↓	↓	↓
	4500	-1125		.30	1.3	1.1	↓	1.0	.8
	4000	-1000		.30	1.4	↓	↓	↓	↓
	3800	-950		.45	1.4	↓	↓	↓	↓
	3700	-925		.72	1.3	1.0	↓	↓	↓
	3600	-900		1.05	1.3	1.0	↓	↓	↓
	3500	-875		1.50	1.6	1.2	↓	↓	↓
	3200	-800		3.55	1.3	1.0	↓	↓	↓
	3000	-2000		.42	1.8	1.3	↓	1.1	.6
	2700	-1800		2.1	1.8	1.3	↓	1.1	.6

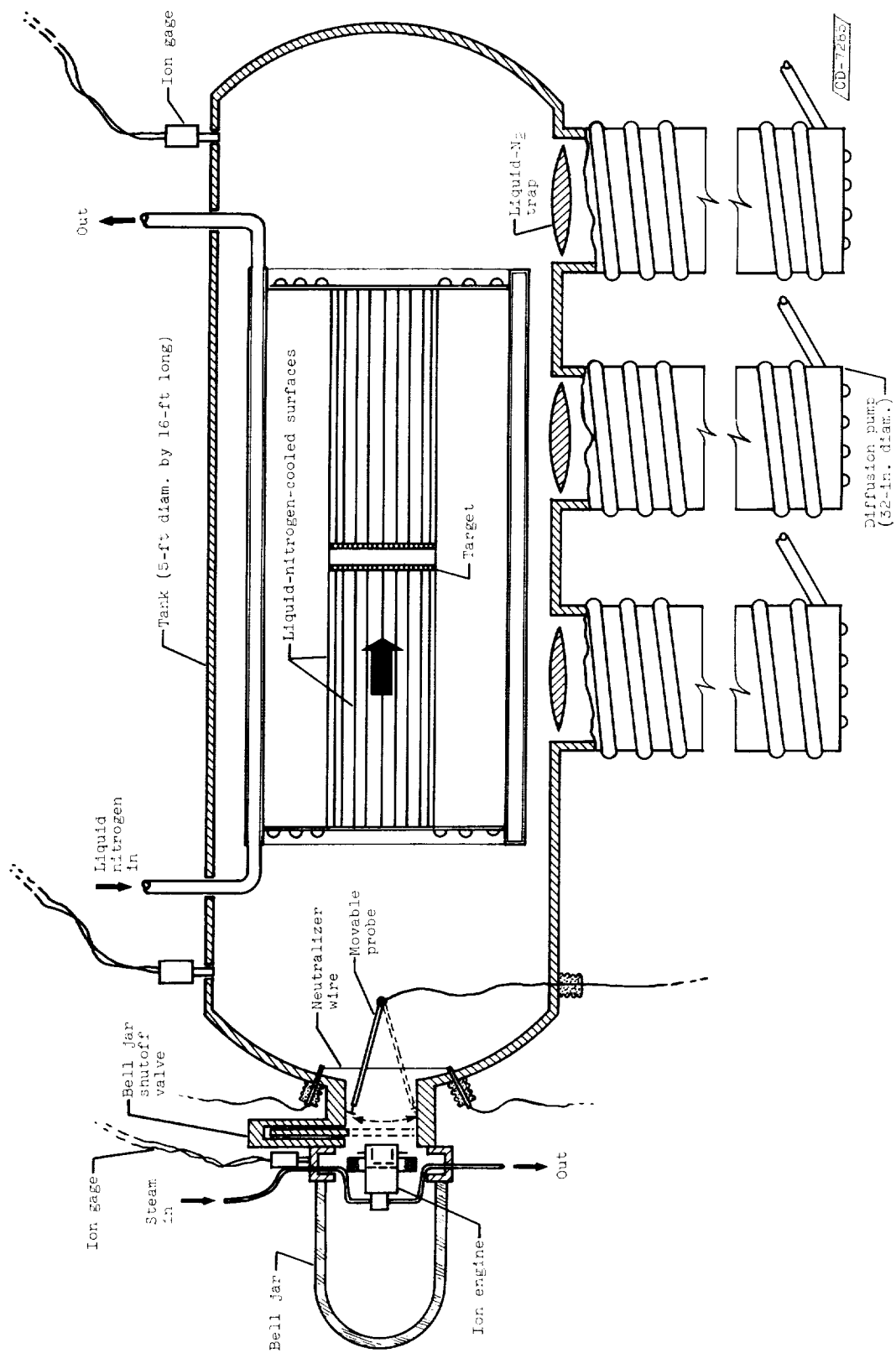


Figure 1. - Ion engine installation and vacuum tank facility.

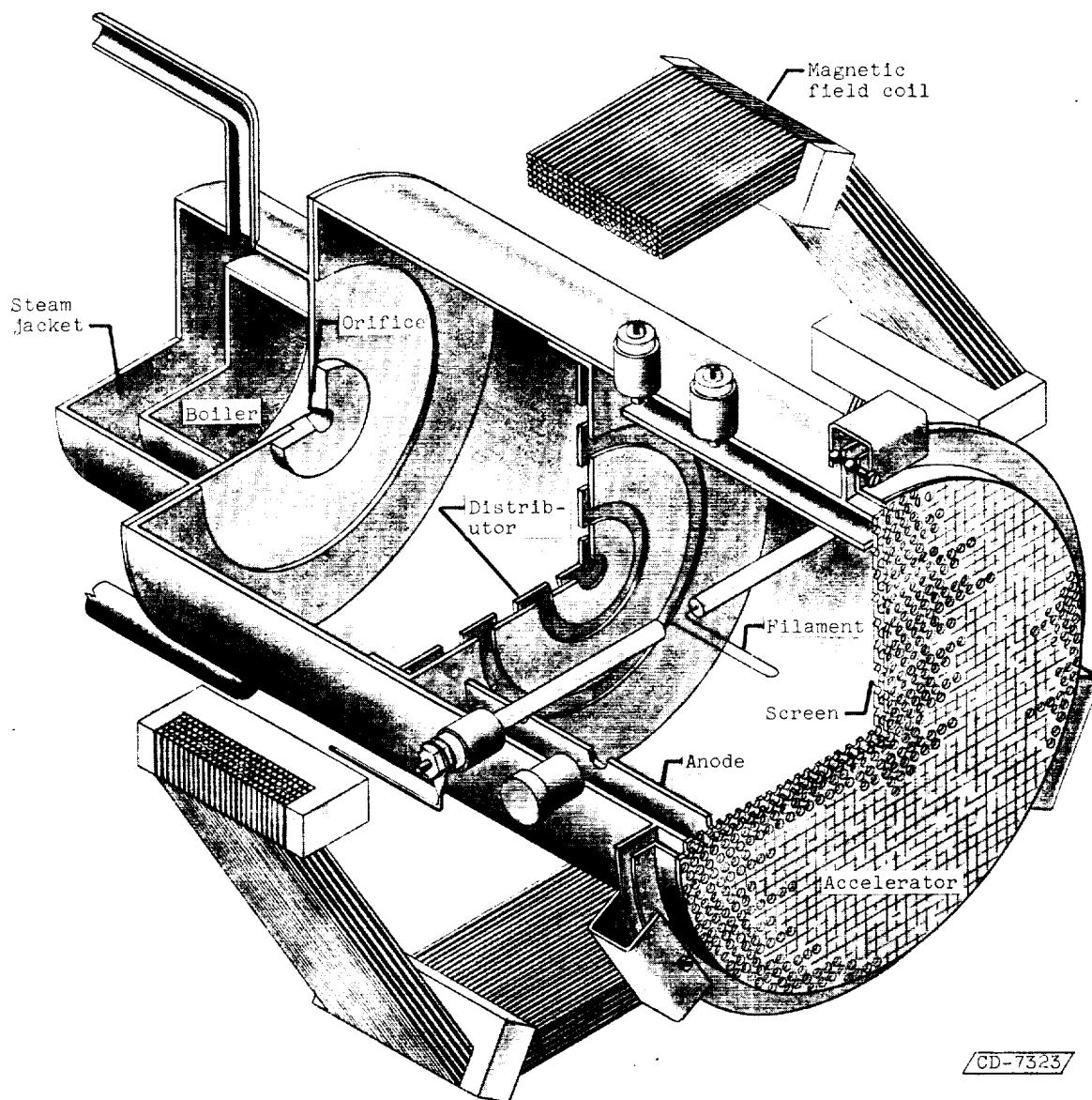
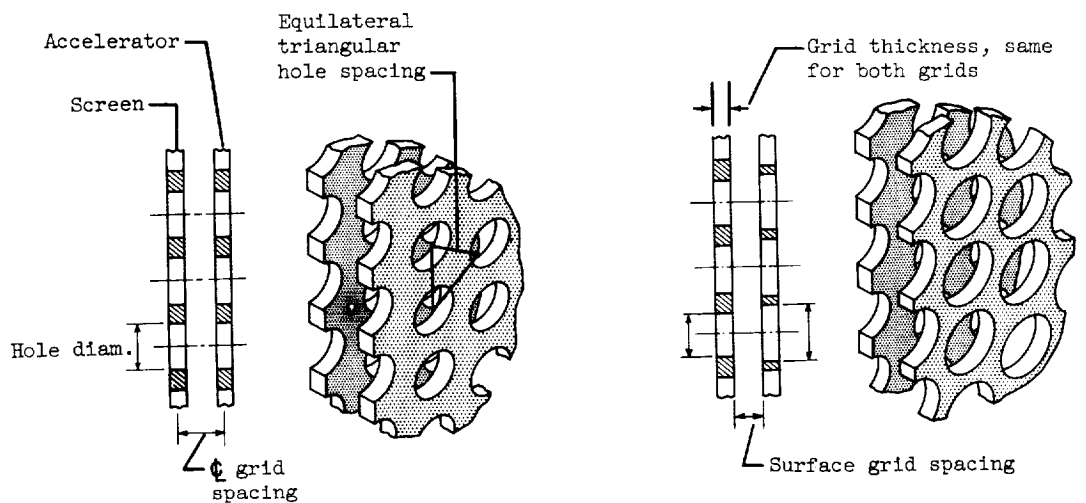
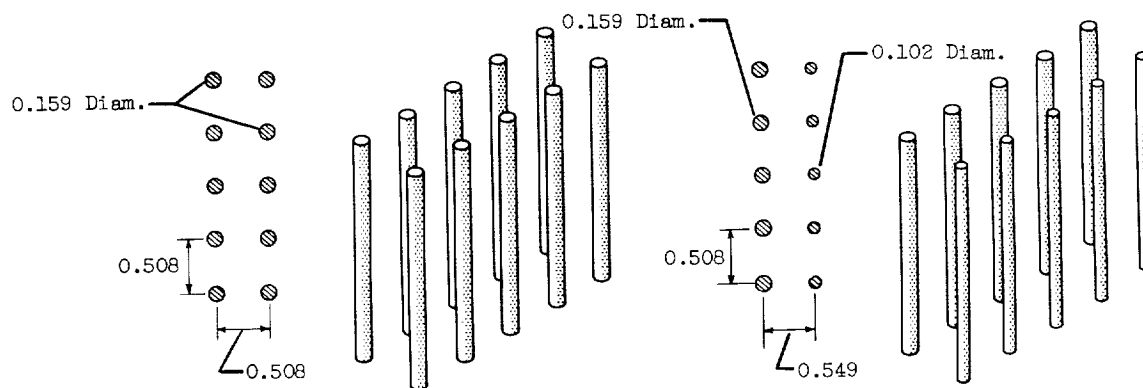


Figure 2. - Cutaway sketch of 10-centimeter-diameter electron-bombardment engine.

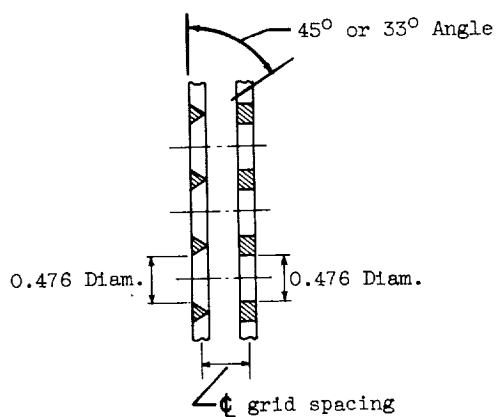


(a) Same holes in both grids.

(b) Larger holes in accelerator.



(c) Parallel grid wire, configurations 12 and 13.

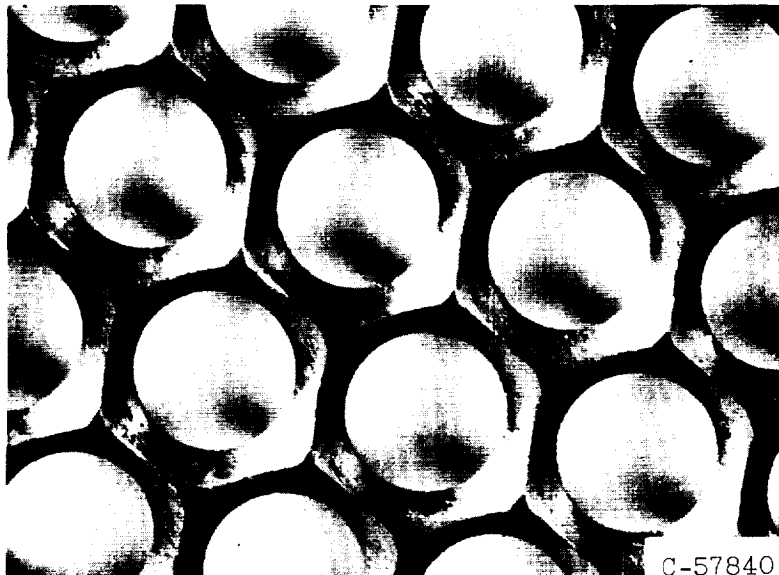


(d) Configuration 14 or 15.

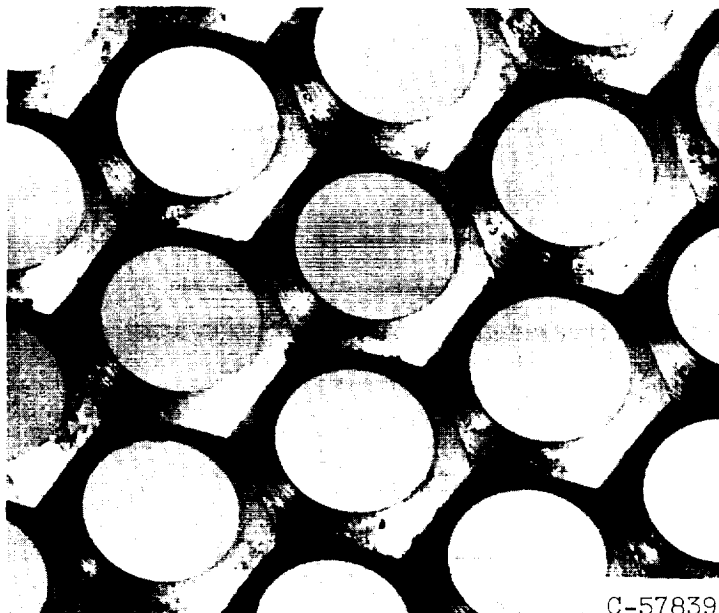
Figure 3. - Details of screen and accelerator grids for a 10-centimeter-diameter electron-bombardment engine. (All dimensions in cm.)



E-1430



(e) Enlarged photograph of  $45^\circ$  screen angle, 0.476-centimeter hole diameter.



(f) Enlarged photograph of  $33^\circ$  screen angle, 0.476-centimeter hole diameter.

Figure 3. - Concluded. Details of screen and accelerator grids for a 10-centimeter-diameter electron-bombardment engine. (All dimensions in cm.)

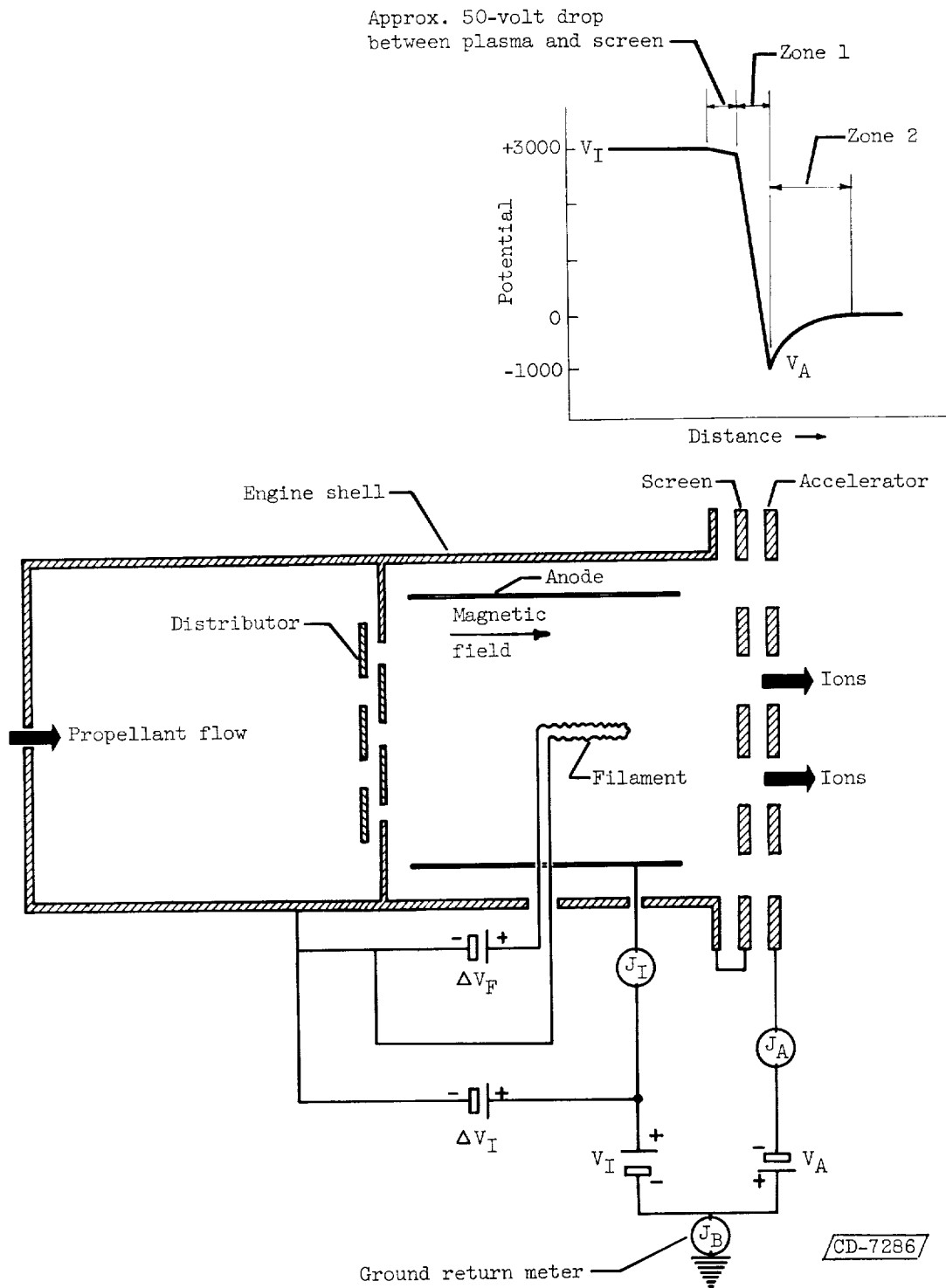
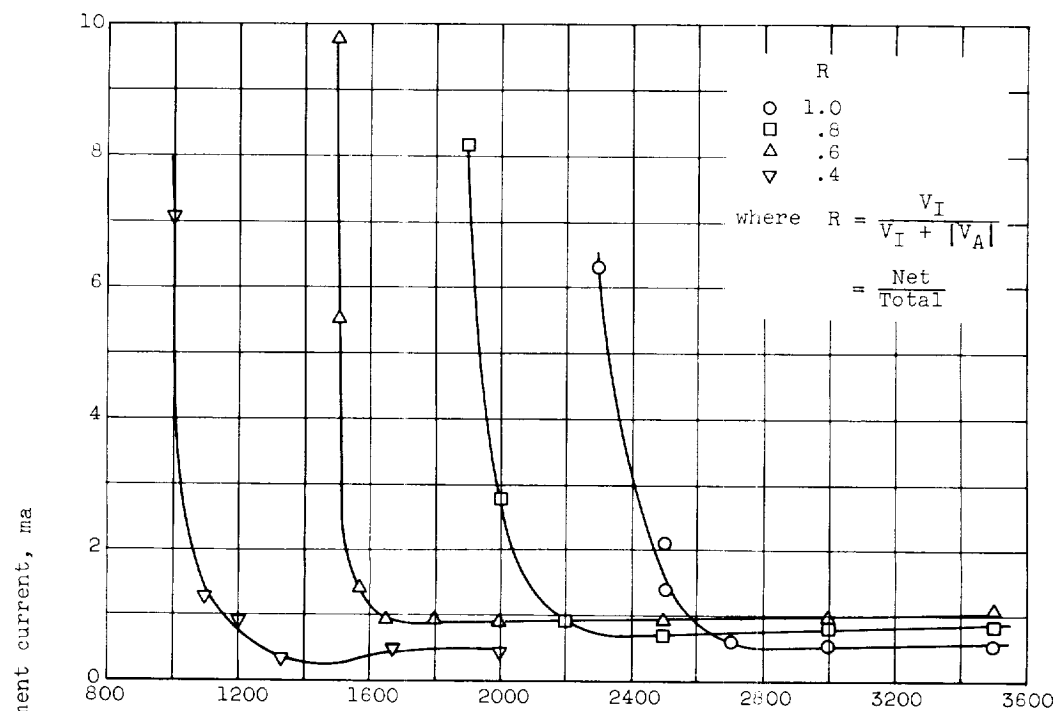
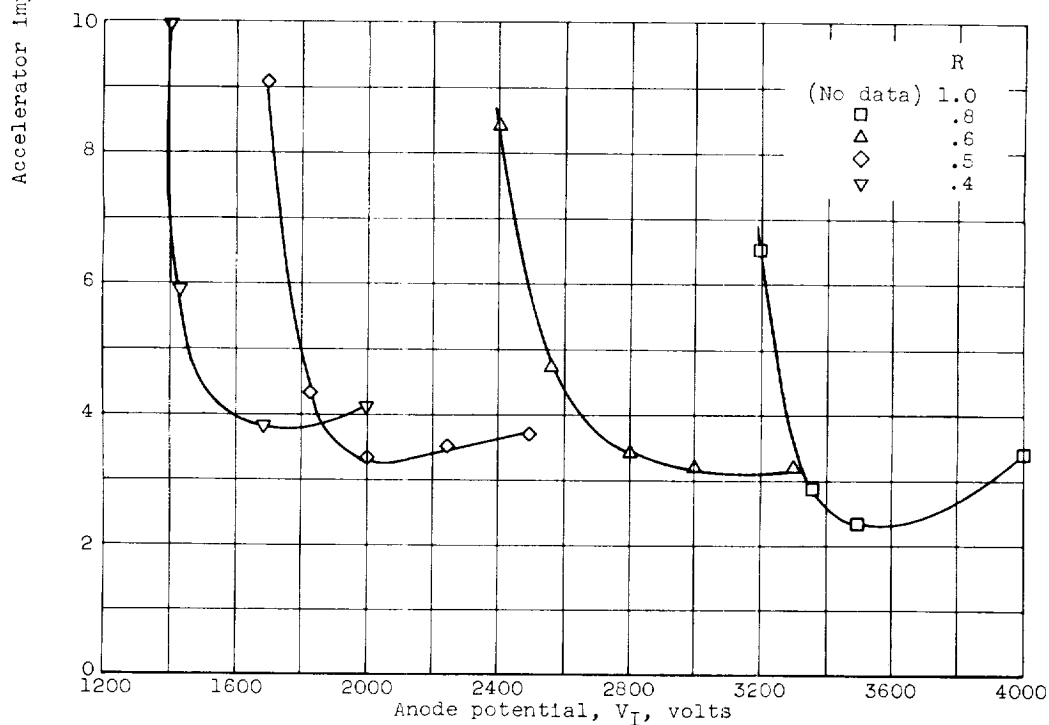


Figure 4. - Schematic electrical diagram and potential profile of ion engine with an electron-bombardment ion source.

E-1430



(a) Beam current, 0.125 ampere.



(b) Beam current, 0.241 ampere.

Figure 5. - Typical data of accelerator impingement currents versus anode potential for 10-centimeter-diameter ion source using number 6 grids.

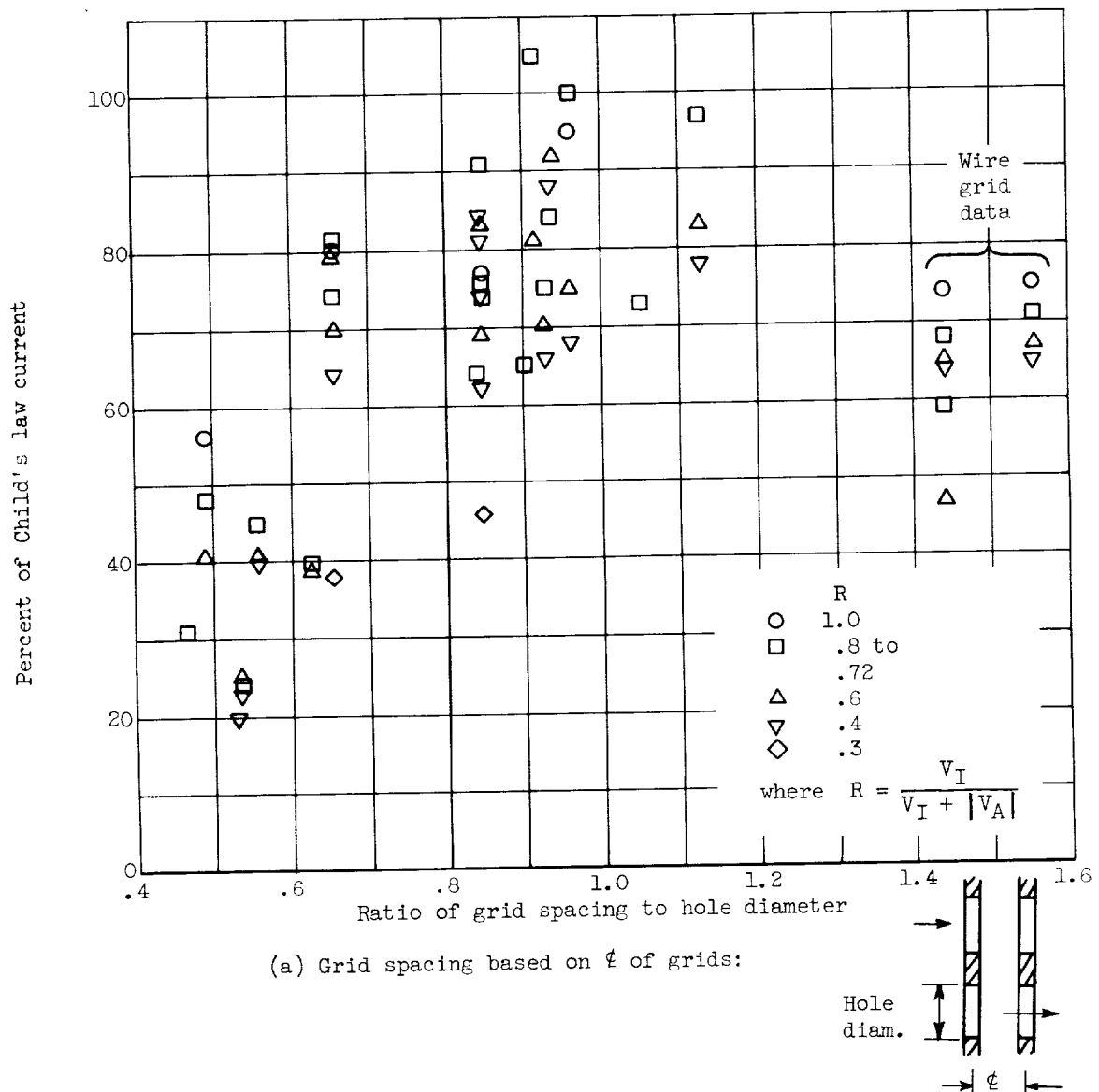


Figure 6. - Percent of Child's law current passing through screen-accelerator grids of a 10-centimeter-diameter rocket. Beam current generally 1/4 or 1/8 ampere; see table II for grid configurations.

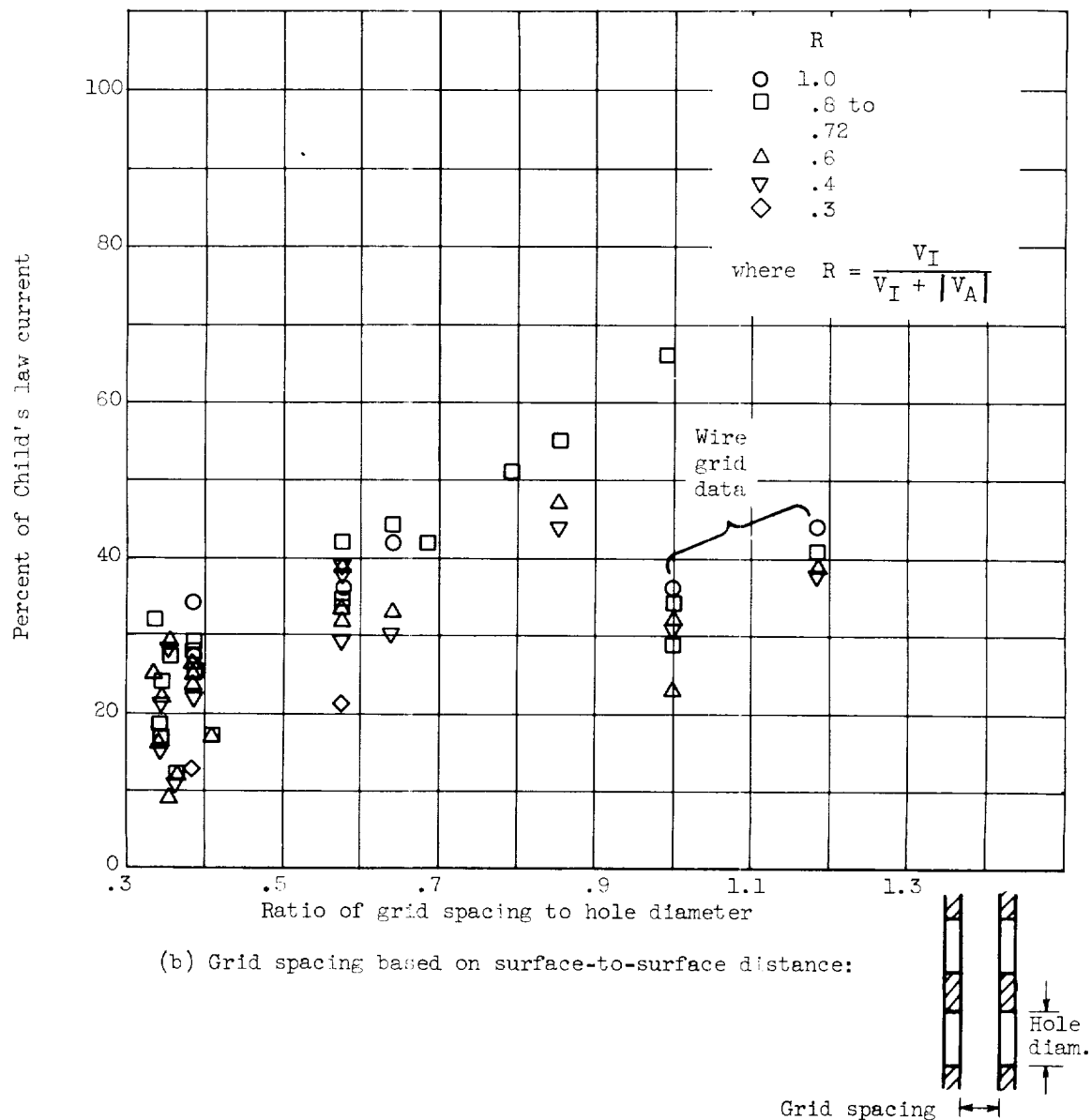


Figure 6. - Concluded. Percent of Child's law current passing through screen-accelerator grids of a 10-centimeter-diameter rocket. Beam current generally 1/4 or 1/8 ampere; see table II for grid configurations.

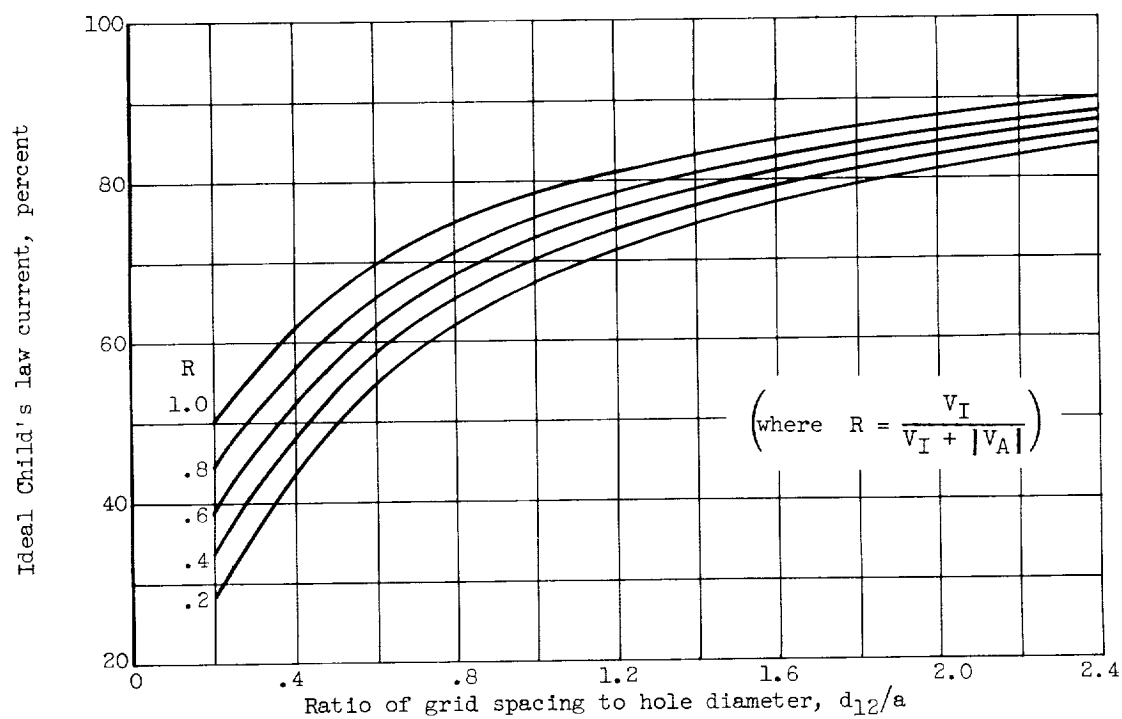


Figure 7. - Calculated value of Child's law current passing through screen-accelerator grids of a 10-centimeter-diameter ion rocket. (Grid aperture effect, appendix B.)

E-1430

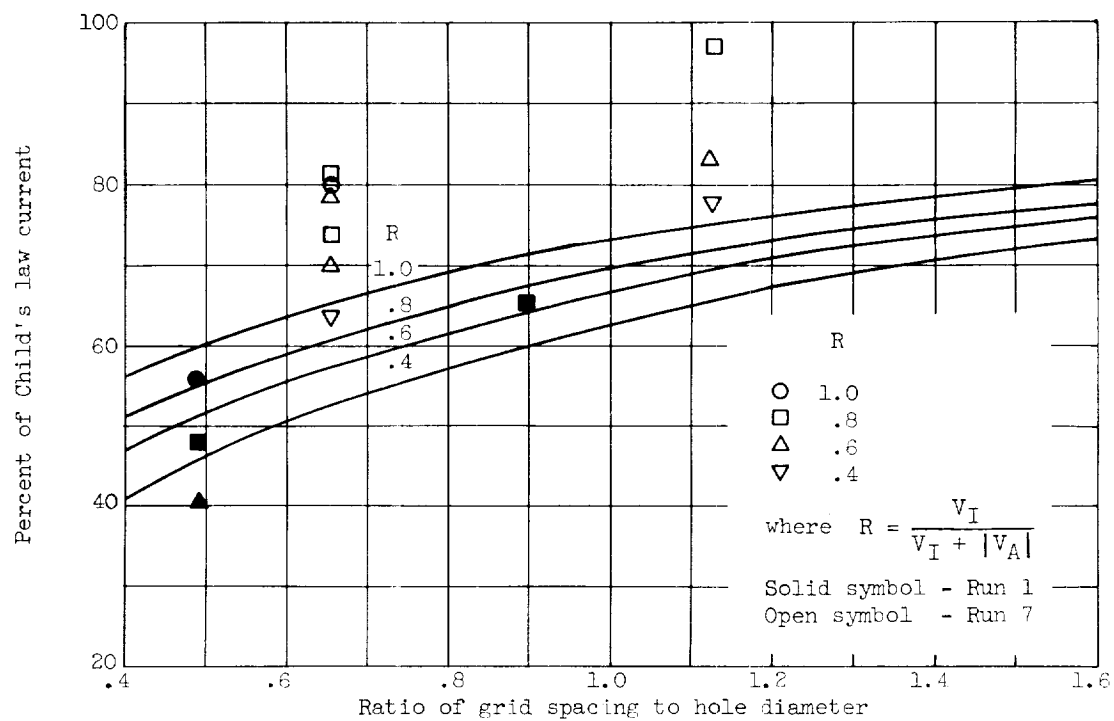


Figure 8. - Comparison of data for grid configurations 1 and 7 with calculated grid aperture effect.

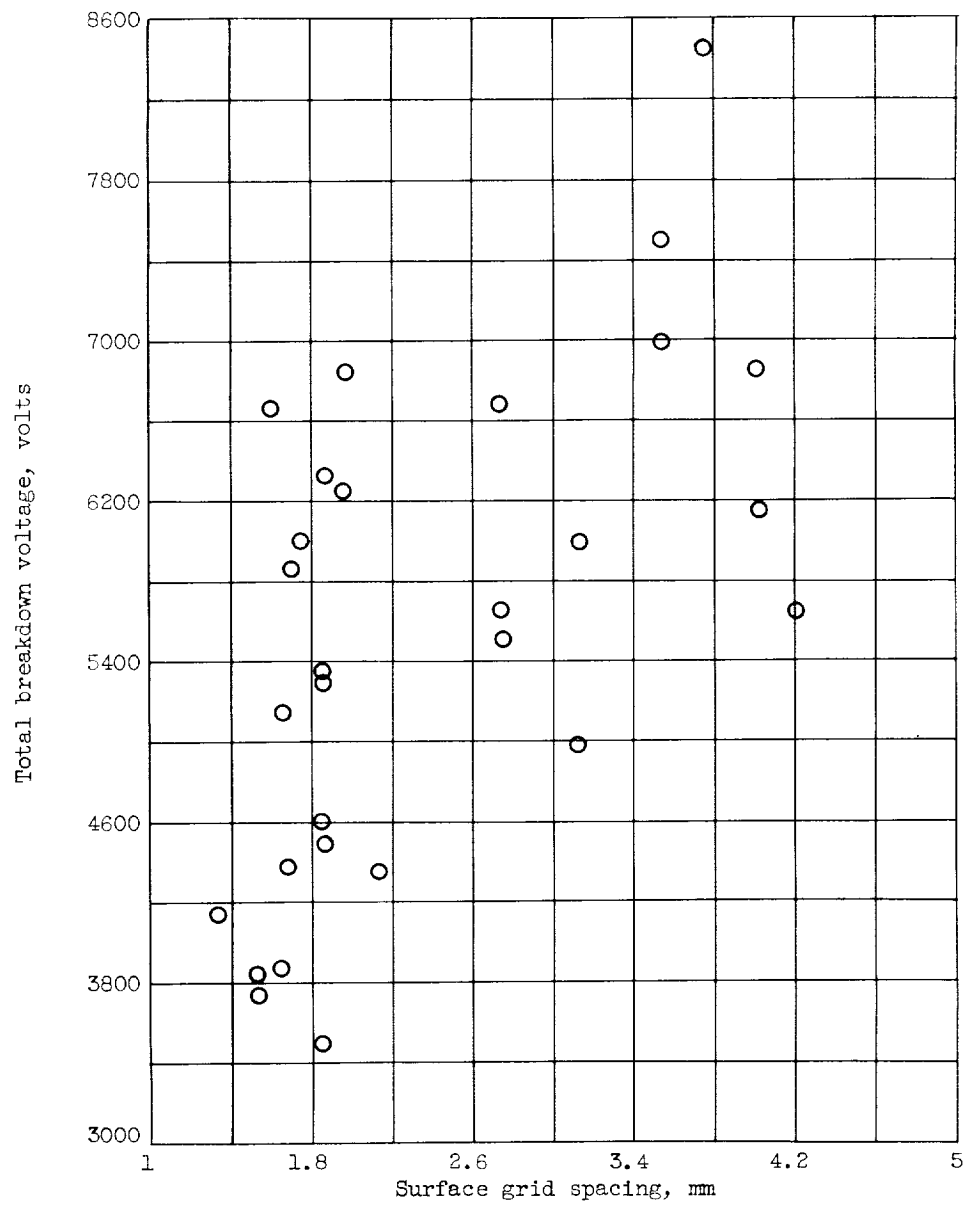


Figure 9. - Breakdown voltage across screen-accelerator grids of an operating 10-centimeter-diameter ion engine. Beam currents, 0.12 to 0.46 ampere; bell jar pressure,  $1 \times 10^{-5}$  to  $3.3 \times 10^{-5}$  mm Hg.



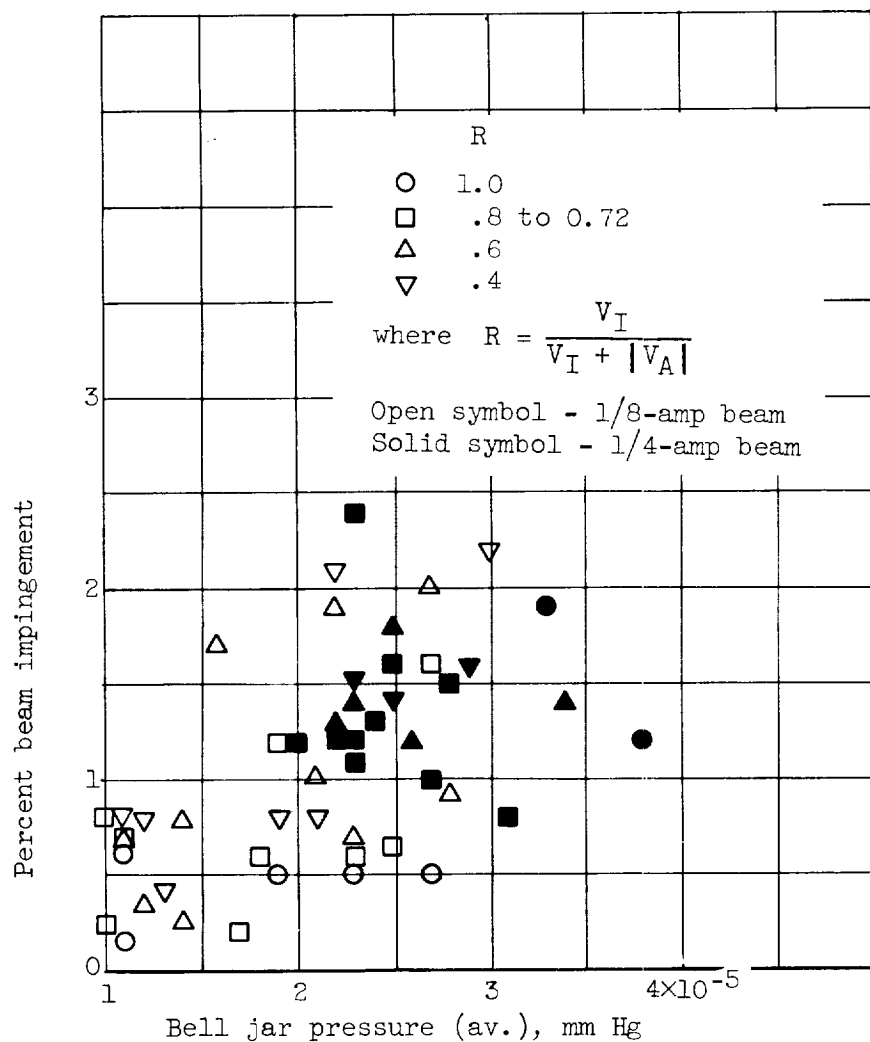


Figure 10. - Percent of beam current impinging on accelerator grid of a 10-centimeter-diameter ion engine as a function of surrounding pressure indicated by the bell jar ion gage.

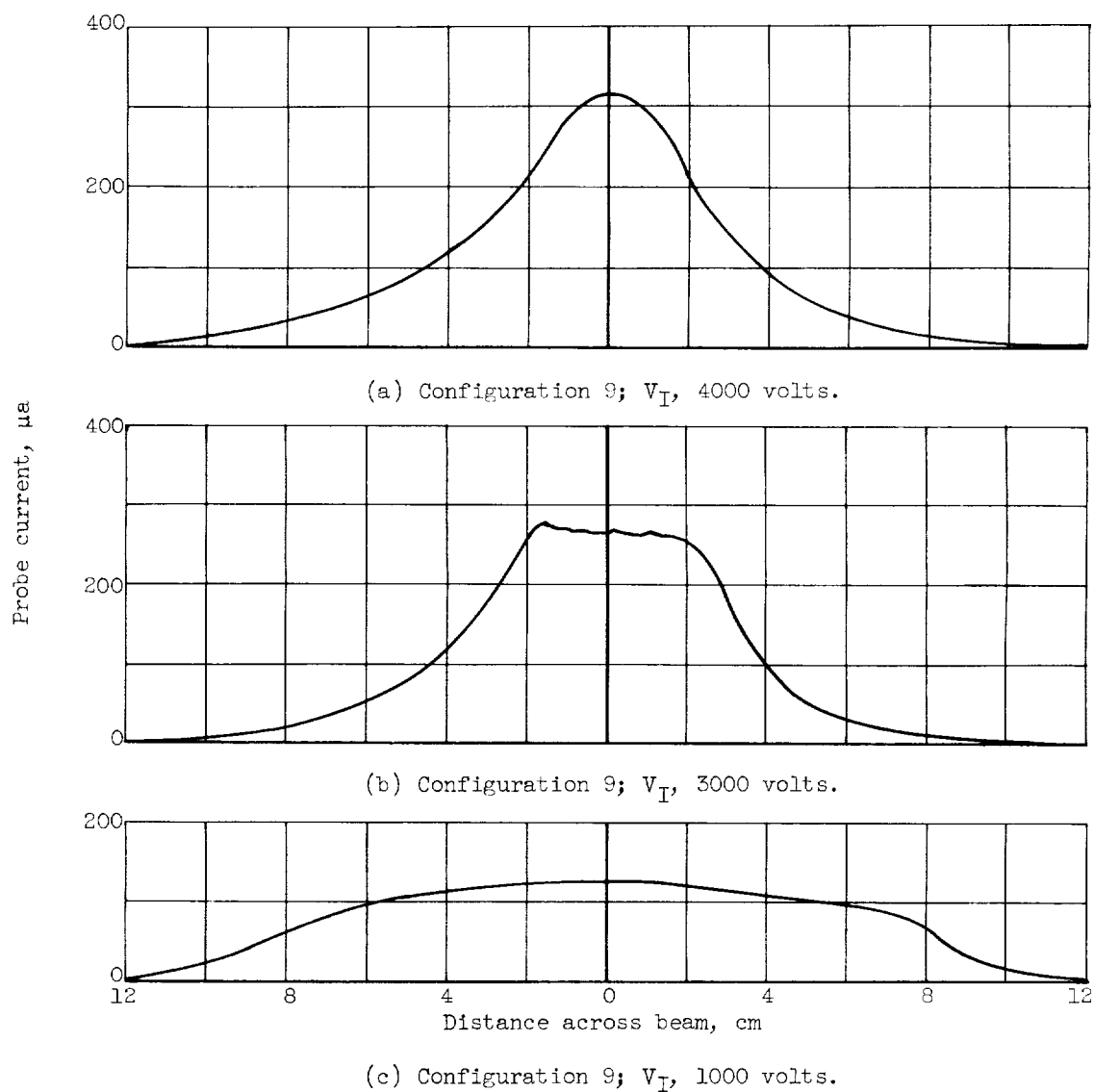


Figure 11. - Beam profile curves generated by molybdenum-tipped probe 12 centimeters downstream of a 10-centimeter-diameter ion engine.  $J_B$ , 0.125 ampere;  $R$ , 0.8 for all profiles.

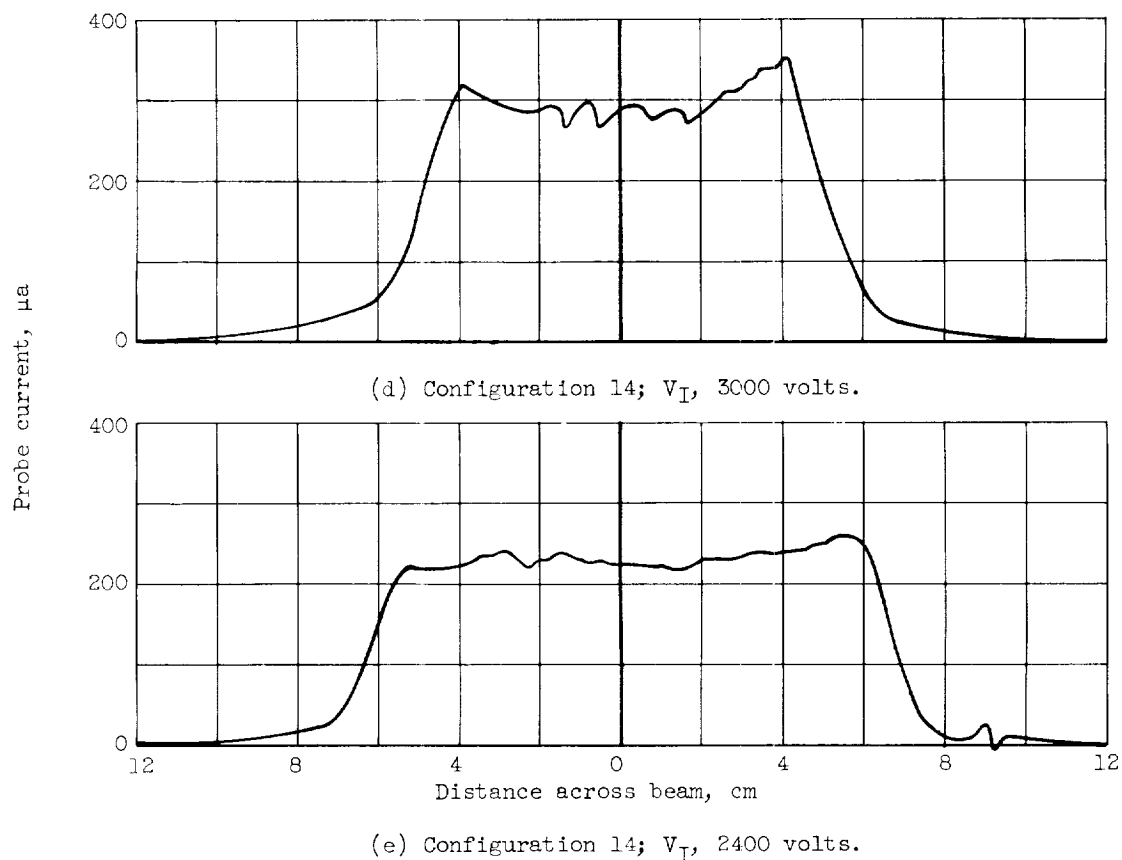


Figure 11. - Concluded. Beam profile curves generated by molybdenum-tipped probe 12 centimeters downstream of a 10-centimeter-diameter ion engine.  $J_B$ , 0.125 ampere;  $R$ , 0.8 for all profiles.

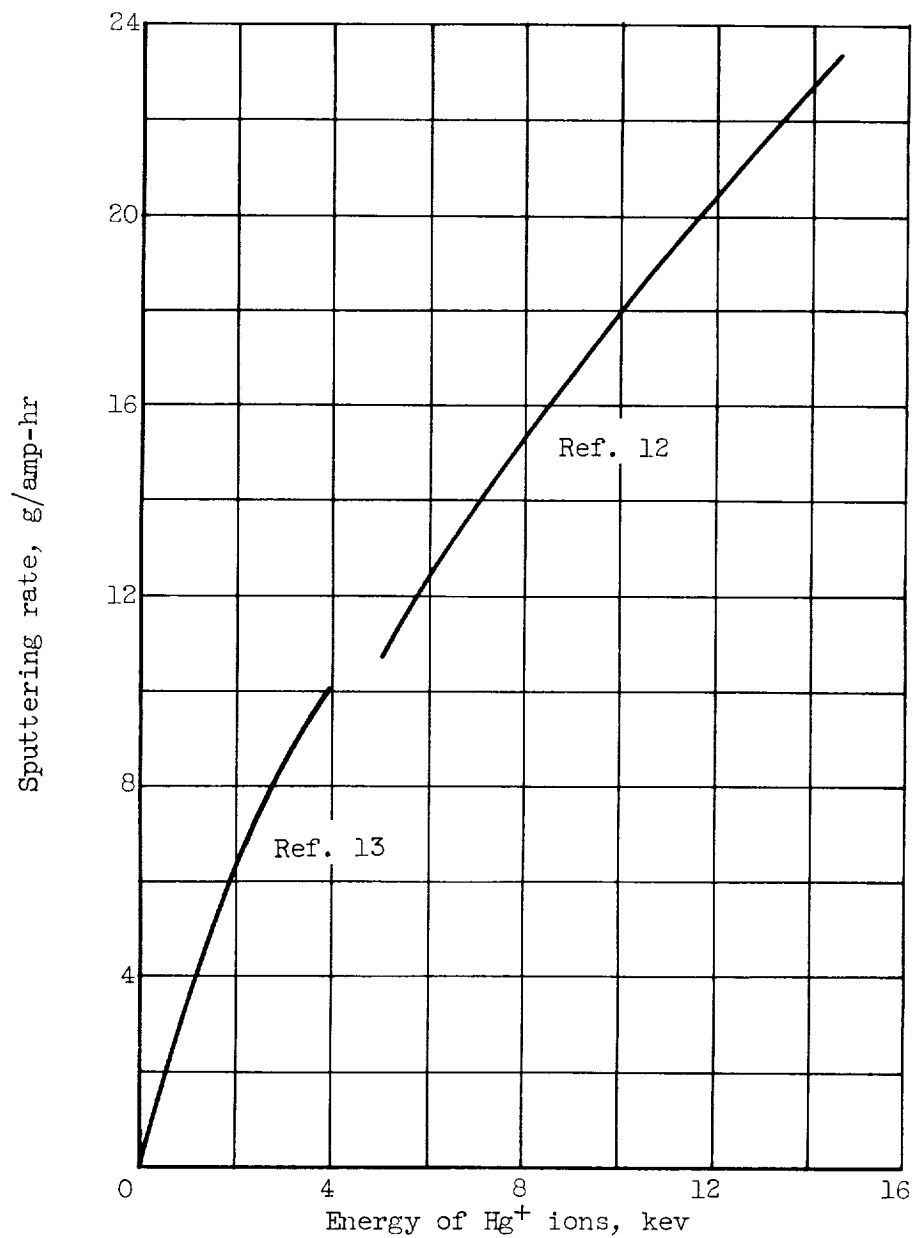


Figure 12. - Sputtering rate of a molybdenum target by singly charged mercury ions (refs. 12 and 13).